A Finite Similitude Approach to Scaled Impact Mechanics

DOI:
10.1016/j.ijimpeng.2020.103744

Document Version
Accepted author manuscript

A Finite Similitude Approach to Scaled Impact Mechanics

Keith Davey[a], Hamed Sadeghi[b], Rooholamin Darvizeh[a], Ali Golbaf[b], Abolfazl Darvizeh[b]

[a]Department of Mechanical, Aerospace and Civil Engineering, The University of Manchester, UK.
[b]Department of Mechanical Engineering, University of Guilan, Rasht, Iran.

Abstract

The response characteristics of large-scale structures subjected to impact loading can in principle be determined by scaled experiments. Unfortunately, scaling suffers from *scale effects* and for impact mechanics, the non-scalability of strain rate and strain hardening can diminish the effectiveness of scaled trials. To resolve this difficulty, a new scaling method has recently appeared in the open literature called finite similitude. The theory is founded on the metaphysical concept of space scaling, where the idea is that by expanding or contracting space, changes in the governing mechanics can be assessed.

In this paper the finite-similitude theory is further developed, where it is demonstrated how the constraints imposed by dimensional analysis can be broken. A new form of similarity is introduced but at the cost of requiring two scaled experiments at distinct scales. It is shown however, how the theory is able to combine the information from the two scaled trials to predict outcomes that can be markedly superior to what can be achieved with experiments at a single scale. All scale dependencies are accounted by the theory and consequently the new formulation attempts to capture scale effects, so provides a more realistic approach to scaled experimentation.

Unlike dimensional analysis, the new *first-order finite similitude* theory can simultaneously target two independent physical properties of common dimension (e.g. initial-yield stress and linear strain hardening). The advantage offered by this feature is demonstrated analytically and numerically in the paper with a focus on axisymmetrical tube buckling and energy absorption. The analytical model serves to expound the theory and the numerical highlights its capabilities and the kinds of accuracy achievable with the new approach.

Keywords: scaling; finite similitude; structural impact; scaled experimentation.

1. Introduction

Despite the significant advances in theoretical and numerical modelling, especially in recent years, it is required that huge structures such as trains, ships and aeroplanes are tested experimentally at least in limited numbers [1]. It is well appreciated that testing of such huge structures can be expensive and time consuming. Undoubtedly, advanced numerical methods and theoretical analysis have led to significant reductions in the number of required full-scale tests [1]. Despite this reduction however, large-scale testing poses significant challenges being constrained by practical limitations and the need to recover critical information useful to numerical and theoretical models. Disparities between the model outputs and experimental response are a common feature arising from physical uncertainties and equipment limitations but also due to simplifications made in numerical simulation [2]. Scaled experimentation offers an alternative approach that has the advantage of being relatively cheap and can often be performed under laboratory conditions. However, it is recognised that one of the principal obstacles to scaled experimentation is *scale effects*, which can be so pronounced to make a scaled trial appear almost worthless. Scale effects are those changes in behaviour that take place with scale and are present in all but the simplest of scaled experiments.

The most well-known method for scaling of impact processes is replica scaling [3-5], which is founded on dimensional analysis. This method is restricted to the use of identical materials for full-scale and small-scale tests, which leads to deviations in behaviour due to scale effects linked to the non-scalability of strain rate and consequently leads to what is known as distorted scaled models [3-5]. In an attempt to correct for the non-scalability of strain rate effects, a new method based on the new set of dimensionless numbers (i.e. impact mass, initial impact velocity and dynamic yielding stress) has been developed [1, 6-8]. This approach, which is known as non-direct similitude, involves applying corrections to the impact velocity and impact mass. As recorded in refs. [1] and [6], the response characteristics of a full-scale model made of a perfectly-plastic material were predicted with a good accuracy with this approach. Also, the response behaviour of axially-impacted cylindrical shells manufactured from a perfectly-plastic material was predicted to good accuracy using small-scale models, again by correcting the initial impact velocity. A requirement of the approach however is knowledge of the strain-rate history involved during the impact process, which is needed for the calculation of correction factors; this is a clear impediment [1], [6]. A similar concern arises with the method presented in ref. [7], where the mean value for strain rate must be known in advance in order to implement the method. The difficulty here is that knowing this information can be impossible or at least difficult to determine, especially if complicated structures and processes are involved. A method was presented in ref. [8] in which the velocity correction factor was obtained as a function of the dimensional scaling factor and the exponent in the Norton-Hoff equation. Although this method is restricted to a particular constitutive equation (i.e. the Norton-Hoff constitutive law), an exact match for rigid, perfectly-plastic case studies was obtained. Also, recently a new technique was proposed by Wei and Hu [9] in which apart from adjusting the impact conditions, additional mass was added to components of the model to balance the strain rate effects.

The methods presented in refs. [1, 4-9] are all based on dimensional analysis and are restricted to using identical materials for full-scale and small-scale models. However, "identical materials" when used in what is supposedly pure dimensional scaling can have different material properties [10] at full- and small-scale experiments. An example of this is steel sheets of 0.25 and 1 mm thicknesses showing substantial differences in their true stress-strain curves [10]. Additionally, it is often necessary to use completely different materials in the small-scale experiments due to different reasons such as manufacturing, costs or experimental restrictions [11]. Thus, it is necessary for developed-scaling theories to be able to account for different material properties pertinent to impact mechanics, which includes density, initial-yield stress, and hardening and strain-rate sensitivity. Despite this requirement, only a few studies have been conducted in the area of impact mechanics that account for different materials and their property differences [11-15]. The study presented in refs. [11] and [14] considered different material properties between the full and small-scale models. Attempts were made to compensate for the differences in density, initial-yield stress and hardening and strain-rate sensitivity by changes in initial conditions such as mass and velocity of impactor. However, these changes proved to be insufficient to return good results since hardening and strain-rate effects were not captured with sufficient accuracy. Best results were returned in refs. [11, 14] for experimental tests on circular plates in which the response behaviour of full-scale plate was predicted with good accuracy using small-scale plates made of same and different materials [15]. The principal difficulty with all the methods discussed thus far is that dimensional analysis provides the underpinning theory, which itself is founded on an invariance principle, i.e. dimensionless governing equations do not change with scale. This can be true in the case of simple experiments, but impact studies are not simple and consequently, distorted models are predominantly the case. This means that ad hoc fixes are necessary to accommodate the fact that dimensionless equations predominantly change in realistic impact studies. Such ad-hoc interventions rarely transfer between different impact scenarios and it is clear that a new direction is needed. The authors contend that a theory called *high-order finite similitude* presented in this paper is the solution to this problem.

The first application of the finite-similitude theory to impact processes was presented by Sadeghi et al. [16] using a version of the theory that is now termed *zeroth-order finite similitude* [17] in preparation for what is to follow. In reference [16] the response of a full-scale model was predicted with good accuracy using small-scale models made of same and different materials by capturing the different material properties including density, initial-yield stress, strain hardening and strain-rate effects. Also, a method was presented by Sadeghi et al. [18] based on the zeroth-order finite similitude theory [17] for scaling of thermo-mechanical impact processes in which damage/failure for first time was scaled. The presented method for scaling of impact processes was verified in ref. [2] experimentally by conducting experiments on axially impacted tubes in which it was revealed that scaled experimentation can provide better predictions compared with sophisticated numerical tools such as Abaqus.

Zeroth-order finite similitude and dimensional analysis have one thing in common, which is that both involve proportional physical fields; assumed for dimensional analysis ab initio and for finite similitude arising as a consequence of the assumption that projected transport equations do not change with scale (more on this in subsequent sections). This restriction manifests practically in zeroth-order similitude theory [16, 18], being unable to simultaneously fix two different physical properties having the same units by means of two different degrees of freedom. The simultaneous fixing of initial-yield stress and hardening for example is an open problem. In the presented paper the high-order finite similitude theory is introduced, and the first-order theory is applied as a first step to gauge what improvements can be gained. The first-order theory uses two scaled experiments at distinct scales, and in many respects the reason for adding one or more scaled experiment is readily appreciated. Scaled experiments capture certain information about the full-scale process and should scale effects be present, then changes in behaviour will be visible at different scales. In order to make use of the different behaviours that appear with scale, it is necessary to have a theory that can combine the information. Patently, dimensional analysis cannot do this, as by design, it assumes no change is taking place.

The theoretical background of the first order finite similitude theory is presented in Section 2. The foundation of the finite-similitude approach is the metaphysical concept of space scaling, which is re-presented in Section 2.1. Note that a "metaphysical" process is defined here to be a process that cannot be realised practically but can nonetheless be imagined and mathematically defined. By means of this imagined space transformation trial-space impact mechanics is projected onto the full-scale physical space. This step is critical as it reveals all scale dependencies that occur in impact mechanics and the issue is examined in Section 2.2. The approach offers great flexibility as scaling effectively reduces to discovering what the space dependencies are; the approach adopted to discover these is the application of global-scale invariances as presented in Section 2.3. As discussed in Section 2.4, a particular choice of invariance provides the *first-order finite similitude* theory and reveals field identities that connect behaviours across the trial experiments and the physical process under scrutiny. The practical implementation of the approach is examined in Section 3, where a procedure for setting the scaling parameters is presented. The testing of the method is undertaken in Section 4 using numerical and analytical approaches for the analysis of axially-impacted tubes. The paper concludes with a list of conclusions.

2. Theoretical background

Introduced in this section is the theoretical foundation to the first-order finite-similitude theory leading to a usable scaling method for impact processes. A brief recap of the idea of space scaling and control-volume kinematics is provided in the first subsection. This leads to the critically important concept of projected impact mechanics in transport form, where scaled behaviour is projected to the full scale. The final subsection describes how the first-order theory provides field identities for use in practical testing.

2.1. A brief recap on finite-similitude theory

The basic philosophy behind the finite-similitude theory is described in references [16-18] but it is constructive to briefly recap the ideas here before extending the theory in the field of impact mechanics. The theory is founded on the concept of metaphysical-space scaling, which is a physically intuitive approach, where the investigated structure tied to the space is affected (i.e. is contracted or expanded) by the contraction or expansion of space. In impact mechanics the starting point of any analysis is the identification of inertial frames for the physical and trial spaces. The full-scale process resides in the physical space and the scaled experiment sits in the trial space and the starting point of any analysis is the specification of inertial coordinate systems denoted by $\boldsymbol{x}_{ts}$ and $\boldsymbol{x}_{ps}$, where the subscripts "ts" and "ps" refer to trial and physical space, respectively. For the sake of simplicity, it is assumed here that the coordinate frames (linked to these systems) are orthonormal. Two temporal measures are also involved denoted to be t_{ps} and t_{ts}, which are taken to be absolute to be consistent with the Newtonian mechanics applied in this study. It is assumed further that t_{ps} and t_{ts} are related by the differential relationship $dt_{ts} = g dt_{ps}$, where g is a positive parameter.

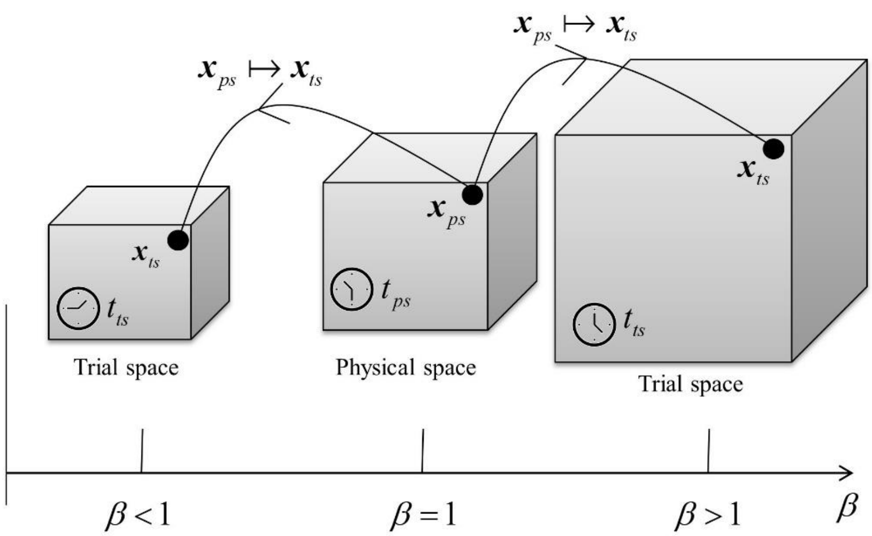

Figure 1. The effect the value of β has on the distortion of space.

Metaphysical scaling is mathematically defined by a temporally invariant affine map, which in differential terms takes the form $d\boldsymbol{x}_{ts} = F \cdot d\boldsymbol{x}_{ps}$ (i.e. $dx^i_{ts} = F^i{}_j dx^j_{ps}$), where the matrix F is both spatially and temporally invariant in view of the focus on scaled experimentation. In this study, the focus is on isotropic scaling, where F adopts a comparatively simple form, i.e. $F = \beta I$, where I is a unit matrix and β is a positive parameter. The effect β has on the physical space is illustrated in Fig. 1, with contraction indicated by $0 < \beta < 1$ and no scaling if $\beta = 1$ and expansion with $1 < \beta$.

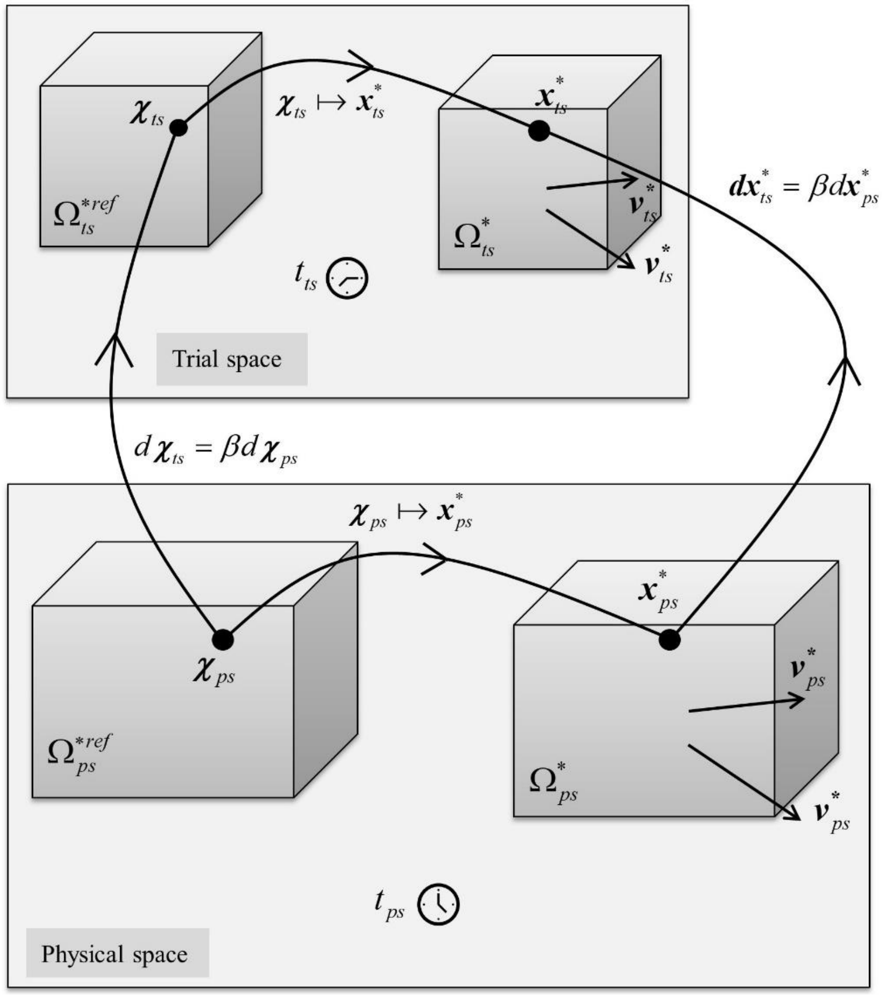

Figure 2. The kinematics of synchronous control volumes Ω^*_{ts} and Ω^*_{ps}.

As described in references [16-18] the finite similitude theory is founded on physics described on synchronised moving controls. The motion of trial-space control volume Ω^*_{ts} can be described mathematically using a velocity field $\boldsymbol{v}^*_{ts}$ and by contrasting its location to a reference control volume Ω^{*ref}_{ts}. The basic idea of synchronised control volume motion in the physical and trial spaces is presented pictorially in Fig. 2. The coordinate point $\boldsymbol{x}^*_{ts}$ is assumed to move with control volume Ω^*_{ts} with velocity $\boldsymbol{v}^*_{ts}$ and in view of the reference control volume Ω^{*ref}_{ts} the following identity applies:

$$\boldsymbol{v}_{ts}^{*} = \frac{D^{*}\boldsymbol{x}_{ts}^{*}}{D^{*}t_{ts}} = \left.\frac{\partial \boldsymbol{x}_{ts}^{*}}{\partial t_{ts}}\right|_{\chi_{ts}} \tag{1}$$

where the derivative $D^{*}/D^{*}t_{ts}$ is used here to signify a temporal derivative with the reference coordinate $\boldsymbol{\chi}_{ts}$ held constant and a similar apparatus applies in the physical space as illustrated in Fig. 2.

The control volume being a region of space is affected by scaling and $d\boldsymbol{x}_{ts}^{*} = \beta d\boldsymbol{x}_{ps}^{*}$ must apply and since $dt_{ts} = g dt_{ps}$ it is evident that synchronous control volumes (i.e. Ω_{ts}^{*} and Ω_{ps}^{*} in Fig. 2) satisfy the velocity relationship $\boldsymbol{v}_{ts}^{*} = g^{-1}\beta \boldsymbol{v}_{ps}^{*}$.

2.2. Projected impact mechanics in transport form

The transport equations for a moving control volume important to impact mechanics for finite similitude are those concerned with volume, continuity, momentum and movement and take the form

$$\frac{D^{*}}{D^{*}t_{ts}} \int_{\Omega_{ts}^{*}} d\Omega_{ts}^{*} - \int_{\Gamma_{ts}^{*}} \boldsymbol{v}_{ts}^{*} \cdot \boldsymbol{n}_{ts} d\Gamma_{ts}^{*} = 0 \tag{2a}$$

$$\frac{D^{*}}{D^{*}t_{ts}} \int_{\Omega_{ts}^{*}} \rho_{ts} d\Omega_{ts}^{*} + \int_{\Gamma_{ts}^{*}} \rho_{ts} \left(\boldsymbol{v}_{ts} - \boldsymbol{v}_{ts}^{*}\right) \cdot \boldsymbol{n}_{ts} d\Gamma_{ts}^{*} = 0 \tag{2b}$$

$$\frac{D^{*}}{D^{*}t_{ts}} \int_{\Omega_{ts}^{*}} \rho_{ts} \boldsymbol{v}_{ts} d\Omega_{ts}^{*} + \int_{\Gamma_{ts}^{*}} \rho_{ts} \boldsymbol{v}_{ts} \left(\boldsymbol{v}_{ts} - \boldsymbol{v}_{ts}^{*}\right) \cdot \boldsymbol{n}_{ts} d\Gamma_{ts}^{*} - \int_{\Gamma_{ts}^{*}} \boldsymbol{\sigma}_{ts} \cdot \boldsymbol{n}_{ts} d\Gamma_{ts}^{*} - \int_{\Omega_{ts}^{*}} \rho_{ts} \boldsymbol{b}_{ts} d\Omega_{ts}^{*} = 0 \tag{2c}$$

$$\frac{D^{*}}{D^{*}t_{ts}} \int_{\Omega_{ts}^{*}} \rho_{ts} \boldsymbol{u}_{ts} d\Omega_{ts}^{*} + \int_{\Gamma_{ts}^{*}} \rho_{ts} \boldsymbol{u}_{ts} \left(\boldsymbol{v}_{ts} - \boldsymbol{v}_{ts}^{*}\right) \cdot \boldsymbol{n}_{ts} d\Gamma_{ts}^{*} - \int_{\Omega_{ts}^{*}} \rho_{ts} \boldsymbol{v}_{ts} d\Omega_{ts}^{*} = 0 \tag{2d}$$

where ρ_{ts} is mass density, $\boldsymbol{v}_{ts}$ is material velocity, $\boldsymbol{u}_{ts}$ is material displacement, $\boldsymbol{\sigma}_{ts}$ is Cauchy stress, $\boldsymbol{n}_{ts}$ is an outward pointing unit normal, $\boldsymbol{b}_{ts}$ is specific-body force (i.e. force per unit mass) and Γ_{ts}^{*} is the boundary of control volume Ω_{ts}^{*}.

The critical equation in impact mechanics is Eq. (2c) but finite similitude involves other considerations that necessitate the involvement of additional equations. In particular, Eq. (2a) is never present in impact studies as it has no field associated with it but is included here to enforce the condition for synchronous control volume motion (i.e. $\boldsymbol{v}_{ts}^{*} = g^{-1}\beta\boldsymbol{v}_{ps}^{*}$). Similarly, the continuity Eq. (2b) is seldom invoked in impact mechanics as density is typically set but is required nevertheless in physical modelling to account for changes in material. Note that Eq. (2d) for movement was first introduced in reference [19] in an attempt to make transport equations more pertinent to solid mechanics since displacement is critical in the description of structural deformation.

With the governing equations and apparatus now in place for space distortion, the most critical step underpinning the finite-similitude theory is now invoked. The projection of Eqs. (2) onto the physical space is critical as it immediately exposes all scale dependencies. The mathematical process involves the substitution of $d\Omega_{ts}^{*} = \beta^{3} d\Omega_{ps}^{*}$, $\boldsymbol{n}_{ts} d\Gamma_{ts}^{*} = \beta^{2}\boldsymbol{n}_{ps} d\Gamma_{ps}^{*}$, $dt_{ts} = g\,dt_{ps}$ into Eqs. (2) along with multiplication throughout by g and non-zero scaling parameters α_0^1, α_0^ρ, α_0^v and α_0^u, respectively. These operations provide the following four important equations:

$$\alpha_0^1 T_0^1\left(\beta\right) = \frac{D^*}{D^* t_{ps}} \int_{\Omega_{ps}^*} \alpha_0^1 \beta^3 d\Omega_{ps}^* - \int_{\Gamma_{ps}^*} \alpha_0^1 \beta^3 \boldsymbol{v}_{ps}^* \cdot \boldsymbol{n}_{ps} d\Gamma_{ps}^* = 0 \tag{3a}$$

$$\alpha_0^\rho T_0^\rho\left(\beta\right) = \frac{D^*}{D^* t_{ps}} \int_{\Omega_{ps}^*} \alpha_0^\rho \beta^3 \rho_{ts} d\Omega_{ps}^* + \int_{\Gamma_{ps}^*} \alpha_0^\rho \beta^3 \rho_{ts} \left(\boldsymbol{V}_{ps} - \boldsymbol{v}_{ps}^*\right) \cdot \boldsymbol{n}_{ps} d\Gamma_{ps}^* = 0 \tag{3b}$$

$$\begin{aligned} \alpha_0^v T_0^v\left(\beta\right) = {} & \frac{D^*}{D^* t_{ps}} \int_{\Omega_{ts}^*} \left(\alpha_0^v g^{-1}\beta\right) \beta^3 \rho_{ts} \boldsymbol{V}_{ps} d\Omega_{ts}^* + \int_{\Gamma_{ps}^*} \left(\alpha_0^v g^{-1}\beta\right) \beta^3 \rho_{ts} \boldsymbol{V}_{ps} \left(\boldsymbol{V}_{ts} - \boldsymbol{v}_{ps}^*\right) \cdot \boldsymbol{n}_{ps} d\Gamma_{ps}^* \\ & - \int_{\Gamma_{ps}^*} \alpha_0^v g \beta^2 \boldsymbol{\sigma}_{ts} \cdot \boldsymbol{n}_{ps} d\Gamma_{ps}^* - \int_{\Omega_{ps}^*} \alpha_0^v g \beta^3 \rho_{ts} \boldsymbol{b}_{ts} d\Omega_{ps}^* = 0 \end{aligned} \tag{3c}$$

$$\begin{aligned} \alpha_0^u T_0^u\left(\beta\right) = {} & \frac{D^*}{D^* t_{ps}} \int_{\Omega_{ps}^*} \left(\alpha_0^u \beta\right) \beta^3 \rho_{ts} \boldsymbol{U}_{ps} d\Omega_{ps}^* + \int_{\Gamma_{ts}^*} \left(\alpha_0^u \beta\right) \beta^3 \rho_{ts} \boldsymbol{U}_{ps} \left(\boldsymbol{V}_{ps} - \boldsymbol{v}_{ps}^*\right) \cdot \boldsymbol{n}_{ps} d\Gamma_{ps}^* \\ & - \int_{\Omega_{ps}^*} \left(\alpha_0^u \beta\right) \beta^3 \rho_{ts} \boldsymbol{V}_{ps} d\Omega_{ps}^* = 0 \end{aligned} \tag{3d}$$

where $\boldsymbol{V}_{ps} = \beta^{-1} g \boldsymbol{v}_{ts}$ and $\boldsymbol{U}_{ps} = \beta^{-1}\boldsymbol{u}_{ts}$.

Eqs. (3) capture all scale dependencies that feature in scaled-impact mechanics, with the appearance of explicit geometrical measures (e.g. β^3 and β^2) but also other hidden dependencies such as the fields $\boldsymbol{V}_{ps}(\beta)$ and $\boldsymbol{U}_{ps}(\beta)$. The scaling problem has effectively been transformed into one where the objective is now to discover the behaviour of the hidden-field dependencies. The theory embraces the presence of scale effects rather than simply ignoring them as is done in dimensional analysis and zeroth-order finite similitude (see refs. [16-18]), which is equivalent to stating that Eqs. (3) are independent of β. There exist two possible options for revealing hidden dependencies, with one requiring additional information (i.e. boundary conditions, size effects etc.), and the other is the application of a global-scale invariance. This latter approach is the focus here as is particularly suited to physical modelling, where the idea is to select a physical invariance that facilitates the design of physical-trial experiments.

2.3. Scale invariances and the first-order theory

Observe that Eqs. (3) are of the form $\alpha_0^\psi T_0^\psi = 0$, with ψ set to 1, ρ, v and u. As mentioned above a particularly obvious β–invariance (and one that has been applied repeatedly for over 100 years) is that $\alpha_0^\psi T_0^\psi(\beta)$ does not depend on β. Written in mathematical terms the requirement is that the identity

$$\frac{d}{d\beta}\left(\alpha_0^\psi T_0^\psi\right) \equiv 0 \tag{4}$$

applies, where the equality sign "$\equiv$" signifies that the derivative is identically zero.

Zeroth-order finite similitude refers to a system of transport equations that satisfies this particular identity and details on its application can be found in references [2, 16-18, 20-22]. The derivation of the identities $\rho_{ps} = \alpha_0^\rho \beta^3 \rho_{ts}$, $\alpha_0^v = g\beta^{-1}\alpha_0^\rho$ and $\alpha_0^u = \beta^{-1}\alpha_0^\rho$ can be found in these references, so not discussed further here, but nevertheless are taken forward to the next level of finite similitude called *first-order finite similitude*. Scaling parameters $\alpha_0^\psi(\beta)$ have the function of attempting to eliminate β from $\alpha_0^\psi T_0^\psi(\beta) = 0$ in order for Eq. (4) to apply. This observation suggests that the definition

$$T_1^\psi = \frac{d}{d\beta}\left(\alpha_0^\psi T_0^\psi\right) \tag{5}$$

should be scaled with new set of scaling parameters $\alpha_1^{\psi}(\beta)$ (satisfying $\alpha_1^{\psi}(1)=1$) and consider then the identity

$$T_2^{\psi} = \frac{d}{d\beta}\left(\alpha_1^{\psi} T_1^{\psi}\right) = \frac{d}{d\beta}\left(\alpha_1^{\psi}\frac{d}{d\beta}\left(\alpha_0^{\psi} T_0^{\psi}\right)\right) \equiv 0 \tag{6}$$

which is the scaled invariance for *first-order finite similitude* and note the route to higher forms on considering $\alpha_2^{\psi} T_2^{\psi}(\beta)=0$ and its derivative with respect to β.

Note that zeroth-order finite similitude with this notation is simply $T_1^{\psi} \equiv 0$ and that Eq. (6) is automatically satisfied if zeroth-order conditions are met; clearly this is a desirable feature. Also expanding the derivative on the right-hand side of Eq. (6) gives

$$\frac{d}{d\beta}\left(\alpha_1^{\psi} T_1^{\psi}\right) = \frac{d\alpha_1^{\psi}}{d\beta} T_1^{\psi} + \alpha_1^{\psi}\frac{dT_1^{\psi}}{d\beta} = \frac{d\alpha_1^{\psi}}{d\beta}\frac{d}{d\beta}\left(\alpha_0^{\psi} T_0^{\psi}\right) + \alpha_1^{\psi}\frac{d^2}{d\beta^2}\left(\alpha_0^{\psi} T_0^{\psi}\right) \equiv 0 \tag{7}$$

which is an expansion in terms of the derivatives of $\alpha_0^{\psi} T_0^{\psi}$, which can represent (by means of osculation), any other linear combination of the derivatives of $\alpha_0^{\psi} T_0^{\psi}$ up to the same order at any arbitrary $\beta=\beta_1$.

This feature is sufficient for scaling purposes and confirms that there is little point in seeking alternative identities involving derivatives of $\alpha_0^{\psi} T_0^{\psi}$ to replace Eq. (6). Moreover, the form of Eq. (6) can be readily integrated using divided differences, which provides added justification for its form and this aspect is discussed in the following section. Prior to this however it is convenient to substitute the zeroth-order constraints $\rho_{ps} = \alpha_0^{\rho}\beta^3\rho_{ts}$, $\alpha_0^{v} = g\beta^{-1}\alpha_0^{\rho}$ and $\alpha_0^{u} = \beta^{-1}\alpha_0^{\rho}$ into Eqs. (3) to obtain

$$\alpha_0^{\rho} T_0^{\rho}(\beta) = \frac{D^*}{D^* t_{ps}}\int_{\Omega_{ps}^*}\rho_{ps}\, d\Omega_{ps}^* + \int_{\Gamma_{ps}^*}\rho_{ps}\left(\boldsymbol{V}_{ps} - \boldsymbol{v}_{ps}^*\right)\cdot\boldsymbol{n}_{ps}\, d\Gamma_{ps}^* = 0 \tag{8a}$$

$$\begin{aligned}\alpha_0^{v} T_0^{v}(\beta) = \frac{D^*}{D^* t_{ps}}\int_{\Omega_{ts}^*}\rho_{ps}\boldsymbol{V}_{ps}\, d\Omega_{ts}^* &+ \int_{\Gamma_{ps}^*}\rho_{ps}\boldsymbol{V}_{ps}\left(\boldsymbol{v}_{ts} - \boldsymbol{v}_{ps}^*\right)\cdot\boldsymbol{n}_{ps}\, d\Gamma_{ps}^* \\ &- \int_{\Gamma_{ps}^*}\boldsymbol{\Sigma}_{ts}\cdot\boldsymbol{n}_{ps}\, d\Gamma_{ps}^* - \int_{\Omega_{ps}^*}\boldsymbol{B}_{ts}\, d\Omega_{ps}^* = 0\end{aligned} \tag{8b}$$

$$\alpha_0^u T_0^u\left(\beta\right)=\frac{D^*}{D^* t_{ps}}\int_{\Omega_{ps}^*}\rho_{ps}\boldsymbol{U}_{ts}d\Omega_{ps}^*+\int_{\Gamma_{ts}^*}\rho_{ps}\boldsymbol{U}_{ps}\left(\boldsymbol{v}_{ps}-\boldsymbol{v}_{ps}^*\right)\cdot\boldsymbol{n}_{ps}d\Gamma_{ps}^*-\int_{\Omega_{ps}^*}\rho_{ps}\boldsymbol{V}_{ps}d\Omega_{ps}^*=0 \qquad (8c)$$

where $\boldsymbol{\Sigma}_{ps}=\alpha_0^v g\beta^2\boldsymbol{\sigma}_{ts}$, $\boldsymbol{B}_{ts}=\alpha_0^v g\beta^3\rho_{ts}\boldsymbol{b}_{ts}=g^2\beta^{-1}\boldsymbol{b}_{ts}$ and where it is noted that Eq. (3a) satisfies Eq. (4) on setting $\alpha_0^1=\beta^{-3}$ and consequently plays no further role in first-order theory. Note that in Eqs. (3) the zeroth-order term $\left(\boldsymbol{v}_{ps}-\boldsymbol{v}_{ps}^*\right)\cdot\boldsymbol{n}_{ps}$ is substituted for $\left(\boldsymbol{V}_{ps}-\boldsymbol{v}_{ps}^*\right)\cdot\boldsymbol{n}_{ps}$ in the momentum and movement equations to avoid the necessity to consider quadratic forms of similitude but also to reflect the fact that the term $\boldsymbol{V}_{ps}\left(\boldsymbol{V}_{ps}\cdot\boldsymbol{n}_{ps}\right)$ tends to be small in solid mechanics.

2.4. First-order field identities

Eq. (6) can be solved numerically by application of divided differences and to ensure an exact representation a mean-value theorem for integration is applied to reveal

$$\alpha_1^\psi \mathrm{T}_1^\psi\left(\beta_2^1\right)\equiv\alpha_1^\psi\left(\beta_2^1\right)\frac{\alpha_0^\psi\mathrm{T}_0^\psi\left(\beta_1\right)-\alpha_0^\psi\mathrm{T}_0^\psi\left(\beta_2\right)}{\beta_1-\beta_2} \qquad (9a)$$

$$\alpha_1^\psi \mathrm{T}_1^\psi\left(\beta_1^0\right)\equiv\alpha_1^\psi\left(\beta_1^0\right)\frac{\alpha_0^\psi\mathrm{T}_0^\psi\left(\beta_0\right)-\alpha_0^\psi\mathrm{T}_0^\psi\left(\beta_1\right)}{\beta_0-\beta_1} \qquad (9b)$$

where $\beta_2\le\beta_2^1\le\beta_1$ and $\beta_1\le\beta_1^0\le\beta_0$ with β_2 and β_1 being scales for trial-space experimentation and $\beta_0=1$ being at full scale as depicted in Fig. 3.

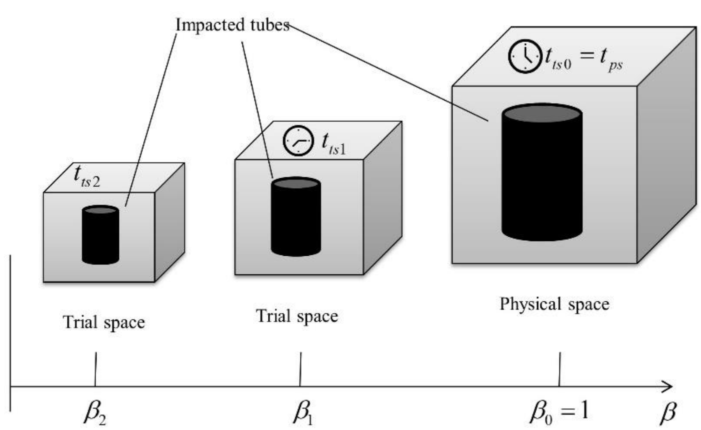

Figure 3. Thin cylindrical tubes in the physical and trial spaces.

In view of Eq. (6) the next divided difference gives zero and consequently $\alpha_1^{\psi} T_1^{\psi}\left(\beta_1^0\right) \equiv \alpha_1^{\psi} T_1^{\psi}\left(\beta_2^1\right)$, which on substitution of Eqs. (9) provides after some manipulation

$$\alpha_0^{\psi} \mathrm{T}_0^{\psi}\left(\beta_0\right) \equiv \alpha_0^{\psi} \mathrm{T}_0^{\psi}\left(\beta_1\right) + R_1^{\psi}\left(\alpha_0^{\psi} \mathrm{T}_0^{\psi}\left(\beta_1\right) - \alpha_0^{\psi} \mathrm{T}_0^{\psi}\left(\beta_2\right)\right) \tag{10}$$

where

$$R_1^{\psi} = \left(\frac{\alpha_1^{\psi}\left(\beta_2^1\right)}{\alpha_1^{\psi}\left(\beta_1^0\right)}\right)\left(\frac{\beta_0 - \beta_1}{\beta_1 - \beta_2}\right) \tag{11}$$

with Eq. (10) providing the sought identity for relating trial-space experiments to the full-scale structure.

Observe here that R_1^{ψ} takes on the role of a parameter due to indeterminacy of α_1^{ψ} and application of Eq. (10) to Eqs. (8) provides the field identities:

$$\boldsymbol{v}_{ps} = \boldsymbol{V}_{ps}\left(\beta_1\right) + R_1^{\rho}\left(\boldsymbol{V}_{ps}\left(\beta_1\right) - \boldsymbol{V}_{ps}\left(\beta_2\right)\right) \tag{12a}$$

$$\boldsymbol{v}_{ps} = \boldsymbol{V}_{ps}\left(\beta_1\right) + R_1^{v}\left(\boldsymbol{V}_{ps}\left(\beta_1\right) - \boldsymbol{V}_{ps}\left(\beta_2\right)\right) \tag{12b}$$

$$\boldsymbol{\sigma}_{ps} = \boldsymbol{\Sigma}_{ps}\left(\beta_1\right) + R_1^{v}\left(\boldsymbol{\Sigma}_{ps}\left(\beta_1\right) - \boldsymbol{\Sigma}_{ps}\left(\beta_2\right)\right) \tag{12c}$$

$$\boldsymbol{b}_{ps} = \boldsymbol{B}_{ps}\left(\beta_1\right) + R_1^{v}\left(\boldsymbol{B}_{ps}\left(\beta_1\right) - \boldsymbol{B}_{ps}\left(\beta_2\right)\right) \tag{12d}$$

$$\boldsymbol{u}_{ps} = \boldsymbol{U}_{ps}\left(\beta_1\right) + R_1^{u}\left(\boldsymbol{U}_{ps}\left(\beta_1\right) - \boldsymbol{U}_{ps}\left(\beta_2\right)\right) \tag{12e}$$

$$\boldsymbol{v}_{ps} = \boldsymbol{V}_{ps}\left(\beta_1\right) + R_1^{u}\left(\boldsymbol{V}_{ps}\left(\beta_1\right) - \boldsymbol{V}_{ps}\left(\beta_2\right)\right) \tag{12f}$$

where to arrive at a consistent velocity expression it is required that $R_1 = R_1^{\rho} = R_1^{v} = R_1^{u}$, which is achieved on setting $\alpha_1^{\rho} = \alpha_1^{v} = \alpha_1^{u}$, and where $\boldsymbol{V}_{ps} = \beta^{-1} g \boldsymbol{v}_{ts}$, $\boldsymbol{U}_{ps} = \beta^{-1} \boldsymbol{u}_{ts}$, $\boldsymbol{\Sigma}_{ps} = \alpha_0^{v} g \beta^2 \boldsymbol{\sigma}_{ts}$ and $\boldsymbol{B}_{ts} = g^2 \beta^{-1} \boldsymbol{b}_{ts}$.

The fields returned by the first-order finite similitude theory are rather elegant in their simplicity as the condition $R_1^{\rho} = R_1^{v} = R_1^{u}$ provides a physically-intuitive solution to Eq. (6). It essentially indicates that the experiments as described by transport Eqs. (8) have proportional differences. The theory provides the fields in Eqs. (12) whose differences are proportional and all that remains is the details of its application. The basic idea is depicted in Fig. 4, where the projection and combination of real trial-space experiments is illustrated. An important feature that is worth noting is that finite-similitude theory does not provide constitutive equations and all the fields required in the physical space are given or can be derived from those in Eqs. (12). However, constitutive equations applied in the physical space can be used to set the scaling parameters and this aspect is discussed in the next section.

3. Practical implementation procedure for impact processes (method)

The high loading rate impact processes are typically described using constitutive equations like Cowper-Symonds and Johnson-Cook, which are not limited to impact processes. In the physical space, the Cowper-Symonds and Johnson-Cook constitutive equations can be presented respectively as [2, 16-18]:

$$\sigma_{ps}^{dyn} = \sigma_{ps}^{stat}\left(1+\left(\frac{\dot{\varepsilon}_{ps}}{D_{ps}}\right)^{\frac{1}{q_{ps}}}\right) \tag{13}$$

$$\sigma_{ps}^{dyn} = \left(A_{ps} + B_{ps}\left(\varepsilon_{ps}^{p}\right)^{n_{ps}}\right)\left(1+C_{ps}\ln\left(\frac{\dot{\varepsilon}_{ps}}{\dot{\varepsilon}_{ps}^{0}}\right)\right) \tag{14}$$

where σ_{ps}^{dyn} is dynamic yield stress, σ_{ps}^{stat} and A_{ps} are initial-yield stress, ε_{ps}^{p} is plastic strain, $\dot{\varepsilon}_{ps}$ and $\dot{\varepsilon}_{ps}^{0}$ are respectively strain rate and reference strain rate and D_{ps}, q_{ps}, B_{ps}, n_{ps} and C_{ps} are determined experimentally.

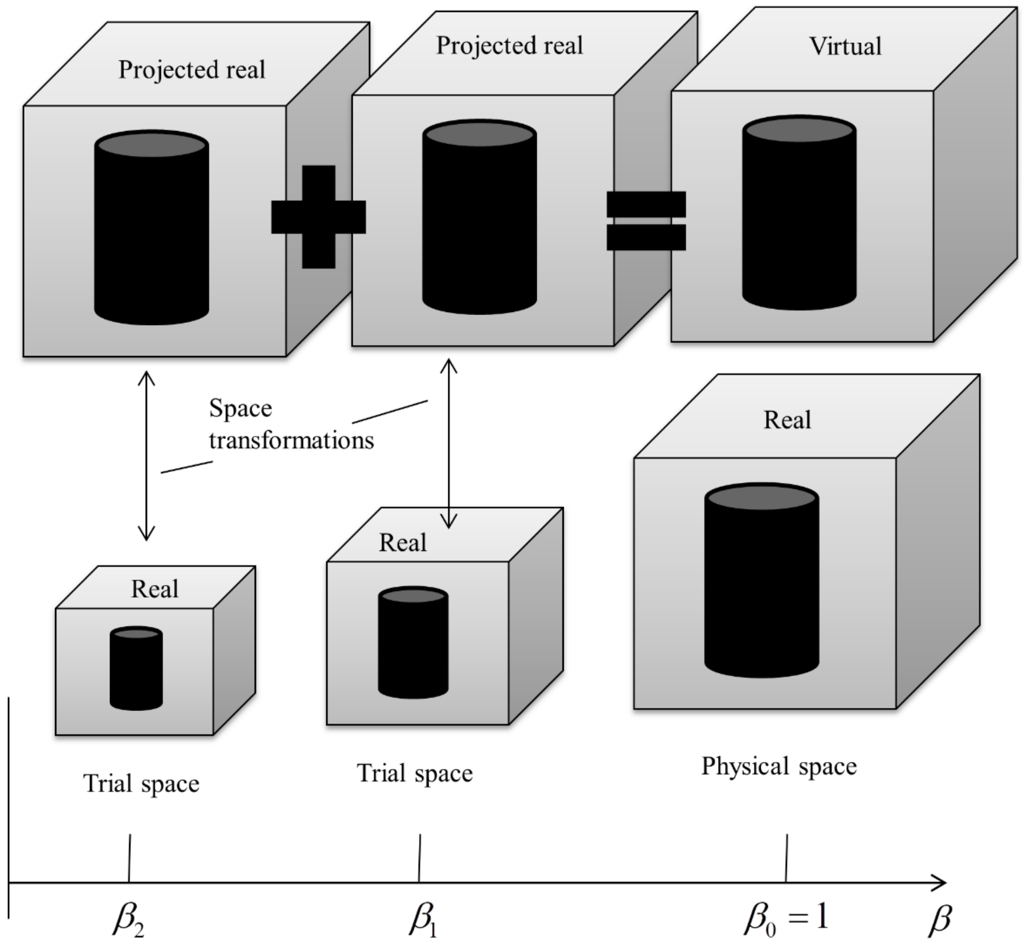

Figure 4. The combination of projected real experiments to form a virtual model.

It is apparent from Eqs. (13) and (14) that the Johnson-Cook constitutive equation accounts for the effects of both strain rate and strain hardening on the yield stress, so is more general than the Cowper-Symonds constitutive equation, which only takes into account the strain-rate effect on the yield stress.

In the trial studies that follow the dimensional scaling parameters β_1 and β_2, are initially set, although the effect of different choices are investigated. Recall the zeroth-order condition $\rho_{ps} = \alpha_0^{\rho} \beta^3 \rho_{ts}$ and recognising that the correct representation of inertial effects in impact processes is of critical importance [2, 11, 16, 18] leads to the following:

$$\alpha_{01}^{\rho} = \frac{1}{\beta_1^3} \frac{\rho_{ps}}{\rho_{ts1}} \tag{15a}$$

$$\alpha_{02}^{\rho} = \frac{1}{\beta_2^3}\frac{\rho_{ps}}{\rho_{ts2}} \tag{15b}$$

where ρ_{ts1} and ρ_{ts2} are the material densities applied in the respective trial spaces.

Zeroth-order conditions are also applied to determine the striking masses in the trial spaces and with α_{01}^{ρ} and α_{02}^{ρ} set by Eqs. (15) these are set by:

$$M_{ts1} = \frac{M_{ps}}{\alpha_{01}^{\rho}} \tag{16a}$$

$$M_{ts2} = \frac{M_{ps}}{\alpha_{02}^{\rho}} \tag{16b}$$

where M_{ps}, M_{ts1} and M_{ts2} respectively represent the striking masses of full-scale model and trial-models 1 and 2. In physical terms Eqs. (16a) and (16b) are attempting to compensate for the differences in mass of the full-scale and trial models as a consequence of the choice made in Eqs. (15), which is achieved by correcting the trial-striking masses.

The next step in setting the scaling parameter is to focus on initial-yield stress and strain hardening. The targeting of these two features of the constitutive curve $\sigma_{ps}^{dyn}\left(\varepsilon_{ps}^{p}, \dot{\varepsilon}_{ps}\right)$ whilst limited to two degrees of freedom (i.e. g_1 and g_2) is achieved by defining two measures, which are:

$$\bar{Y}_{ps} = \frac{1}{\dot{\varepsilon}_{ps}^{\max}} \int_0^{\dot{\varepsilon}_{ps}^{\max}} \sigma_{ps}^{dyn}\left(0, \dot{\varepsilon}_{ps}\right) d\dot{\varepsilon}_{ps} \tag{17a}$$

$$\bar{H}_{ps} = \frac{1}{\varepsilon_{ps}^{p\max}\dot{\varepsilon}_{ps}^{\max}} \int_0^{\varepsilon_{ps}^{p\max}} \int_0^{\dot{\varepsilon}_{ps}^{\max}} \sigma_{ps}^{dyn}\left(\varepsilon_{ps}^{p}, \dot{\varepsilon}_{ps}\right) d\dot{\varepsilon}_{ps} d\varepsilon_{ps}^{p} \tag{17b}$$

where $\bar{Y}_{ps}$ and $\bar{H}_{ps}$ represent mean values of initial-yield and strain hardening.

To show how these measures are applied consider first the first-order identity for stress Eq. (12c) for a uniaxial, which is

$$\sigma_{ps} = \alpha_{01}^{\rho} g_1^2 \beta_1 \sigma_{ts1} + R_1\left(\alpha_{01}^{\rho} g_1^2 \beta_1 \sigma_{ts1} - \alpha_{02}^{\rho} g_2^2 \beta_2 \sigma_{ts2}\right) \tag{18}$$

which on multiplication throughout by $d\varepsilon_{ps}^{p}$ and $d\dot{\varepsilon}_{ps}$, and on application of the following approximations

$$d\varepsilon_{ps}^{p} = \frac{\varepsilon_{ps}^{p\max}}{\varepsilon_{ts1}^{p\max}} d\varepsilon_{ts1}^{p} \tag{19a}$$

$$d\varepsilon_{ps}^{p} = \frac{\varepsilon_{ps}^{p\max}}{\varepsilon_{ts2}^{p\max}} d\varepsilon_{ts2}^{p} \tag{19b}$$

$$d\dot{\varepsilon}_{ps} = \frac{\dot{\varepsilon}_{ps}^{\max}}{\dot{\varepsilon}_{ts1}^{\max}} d\dot{\varepsilon}_{ts1} \tag{19c}$$

$$d\dot{\varepsilon}_{ps} = \frac{\dot{\varepsilon}_{ps}^{\max}}{\dot{\varepsilon}_{ts2}^{\max}} d\dot{\varepsilon}_{ts2} \tag{19d}$$

provides

$$\sigma_{ps} d\dot{\varepsilon}_{ps} d\varepsilon_{ps}^{p} = \alpha_{01}^{\rho} g_1^2 \beta_1 \frac{\varepsilon_{ps}^{p\max}}{\varepsilon_{ts1}^{p\max}} \frac{\dot{\varepsilon}_{ps}^{\max}}{\dot{\varepsilon}_{ts1}^{\max}} \sigma_{ts1} d\dot{\varepsilon}_{ts1} d\varepsilon_{ts1}^{p} + R_1 \left(\alpha_{01}^{\rho} g_1^2 \beta_1 \frac{\varepsilon_{ps}^{p\max}}{\varepsilon_{ts1}^{p\max}} \frac{\dot{\varepsilon}_{ps}^{\max}}{\dot{\varepsilon}_{ts1}^{\max}} \sigma_{ts1} d\dot{\varepsilon}_{ts1} d\varepsilon_{ts1}^{p} - \alpha_{02}^{\rho} g_2^2 \beta_2 \frac{\dot{\varepsilon}_{ps}^{\max}}{\dot{\varepsilon}_{ts2}^{\max}} \frac{\varepsilon_{ps}^{p\max}}{\varepsilon_{ts2}^{p\max}} \sigma_{ts2} d\dot{\varepsilon}_{ts2} d\varepsilon_{ts2}^{p} \right) \tag{20a}$$

$$\sigma_{ps} d\dot{\varepsilon}_{ps} = \alpha_{01}^{\rho} g_1^2 \beta_1 \frac{\dot{\varepsilon}_{ps}^{\max}}{\dot{\varepsilon}_{ts1}^{\max}} \sigma_{ts1} d\dot{\varepsilon}_{ts1} + R_1 \left(\alpha_{01}^{\rho} g_1^2 \beta_1 \frac{\dot{\varepsilon}_{ps}^{\max}}{\dot{\varepsilon}_{ts1}^{\max}} \sigma_{ts1} d\dot{\varepsilon}_{ts1} - \alpha_{02}^{\rho} g_2^2 \beta_2 \frac{\dot{\varepsilon}_{ps}^{\max}}{\dot{\varepsilon}_{ts2}^{\max}} \sigma_{ts2} d\dot{\varepsilon}_{ts2} \right) \tag{20b}$$

where integration between the limits defined in Eqs. (17) gives

$$\bar{H}_{ps} = \alpha_{01}^{\rho} g_1^2 \beta_1 \bar{H}_{ts1} + R_1 \left(\alpha_{01}^{\rho} g_1^2 \beta_1 \bar{H}_{ts1} - \alpha_{02}^{\rho} g_2^2 \beta_2 \bar{H}_{ts2} \right) \tag{21a}$$

$$\bar{Y}_{ps} = \alpha_{01}^{\rho} g_1^2 \beta_1 \bar{Y}_{ts1} + R_1 \left(\alpha_{01}^{\rho} g_1^2 \beta_1 \bar{Y}_{ts1} - \alpha_{02}^{\rho} g_2^2 \beta_2 \bar{Y}_{ts2} \right) \tag{21b}$$

and in order to keep things reasonably simple the following settings are applied: $\dot{\varepsilon}_{ps}^{\max} = g_1 \dot{\varepsilon}_{ts1}^{\max} = g_2 \dot{\varepsilon}_{ts2}^{\max}$, $\varepsilon_{ps}^{p\max} = \varepsilon_{ts1}^{p\max} = \varepsilon_{ts2}^{p\max}$ with $\varepsilon_{ps}^{\max} = 1$ and $\dot{\varepsilon}_{ps}^{\max} = 10/\text{ms}$ to cover the maximum values of plastic strain and strain rate that are likely to take place in a high loading rate impact process [16, 23].

Note that Eqs. (21) provide a system of two equations and three unknowns but in this study R_1 is to be set over a range of values in order to examine its effect on the predictions. Not all values of R_1 lead to reasonable values of g_1 and g_2, however it is shown in the following section that although R_1 affects accuracy it almost always provides more accurate results than those obtained with the zeroth-order method presented in Refs. [2, 16, 18]. Finally by specifying the values of g_1 and g_2, the impact velocities of the trial models are determined using zeroth-order identities:

$$v_{0ts1} = \frac{\beta_1}{g_1} v_{0ps} \tag{22a}$$

$$v_{0ts2} = \frac{\beta_2}{g_2} v_{0ps} \tag{22b}$$

which physically means that differences between initial-yield stress, strain hardening and strain rate of full-scale and trial models are compensated by correcting the initial impact velocities of the trial models. Note that elastic moduli are not targeted in the employed procedure, which is a deficiency if elastic behaviour is significant.

Despite the complexity involved in deriving of the scaling method applicable for high loading rate processes, its application is relatively straightforward as detailed in the following steps:

1. Specify the geometrical and material properties, boundary and initial conditions of (mass and velocity of striking mass) full-scale model;
2. Specify the material properties and boundary conditions (boundary conditions are same as the boundary conditions of the full-scale model) of trial models;
3. Calculate the geometrical properties of trial models by determining the dimensional scaling factors (i.e. β_1 and β_2); also, calculate the density scaling factors (i.e. α_{01}^{ρ} and α_{02}^{ρ}) and the masses of trial models (i.e. M_{ts1} and M_{ts2}) using Eqs. (15)-(16);
4. Calculate the time scaling parameters (i.e. g_1 and g_2) using Eqs. (20)-(21) and setting the R_1 to be equal to any value; then calculate the impact velocities of the trial models using Eqs. (22);
5. Conduct experimental tests on the trial models and use Eqs. (12) to predict the response characteristics of the full-scale model.

The important relationships applied in the practical investigation provided in the next section are:

$$\underline{P}_{ps} = \alpha_{01}^{\rho} g_1^2 \beta_1^{-1} \underline{P}_{ts1} + R_1 \left(\alpha_{01}^{\rho} g_1^2 \beta_1^{-1} \underline{P}_{ts1} - \alpha_{02}^{\rho} g_2^2 \beta_2^{-1} \underline{P}_{ts2} \right) \tag{23a}$$

$$t_{ps} = g_1^{-1} t_{ts1} \tag{23b}$$

$$t_{ps} = g_2^{-1} t_{ts2} \tag{23c}$$

$$\underline{u}_{ps} = \beta_1^{-1} \underline{u}_{ts1} + R_1 \left(\beta_1^{-1} \underline{u}_{ts1} - \beta_2^{-1} \underline{u}_{ts2} \right) \tag{23d}$$

where $\underline{P}$ is force, and where on setting R_1 equal to zero, zeroth-order relationships are returned.

4. Numerical experiments: Results and discussion

In this section, the presented method for scaling of high loading rate processes is tested theoretically and numerically. The tubes impacted axially are selected as case studies since the impact behaviour of tubes involving various deformation mechanisms [2, 16, 24-28] provide a good challenge for testing of the proposed method. Thin-walled tubes have been the subject of many researches over the last two decades [27] and are recognised to be one of the most important energy absorption systems [2, 16, 24-28]. This stems for a few things such as lightness, high energy absorption capacity, a long crushing length and high energy absorption to weight ratio [28]. Numerical results obtained by the finite element software LS-Dyna are compared and validated with reported results in Refs. [2, 25]. LS-Dyna is a commercial software package that is particularly well suited to the simulation of nonlinear and transient dynamic analysis [29]. The presented scaling method is tested in case study I using an analytical relationship for calculating peak loads of axially impacted tubes in which the strain-rate effect is taken into account using Cowper-Symonds constitutive equation. Additionally, in case study II, the theory is tested numerically by simulation of axially impacted tubes in LS-Dyna in which the strain-rate effect is again accounted for using the Cowper-Symonds constitutive equation. Finally, in case study III, the Johnson-Cook constitutive equation is used for investigating both strain-rate and strain-hardening effects. Note that case studies I and II provide evidence that the success of the scaling methodology is not dependent on the solution procedure selected. Similarly, case studies II and III provide evidence that success is not dependent on the constitutive laws adopted.

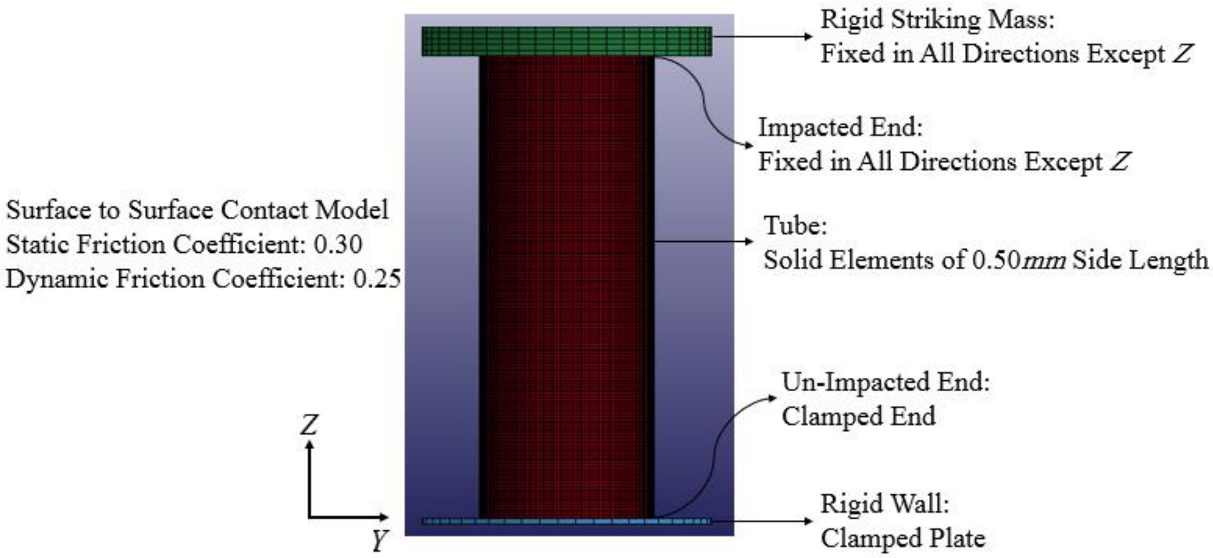

Figure 5. A general figure of axially impacted tube simulated by the LS-Dyna finite element software.

The numerical simulations of axially impacted tubes are conducted using the LS-Dyna finite element software [29]. One-point integration 8-node solid elements of $0.50\ \mathrm{mm}$ side length obtained by a convergence study are used (otherwise the mesh size is specified) in all of simulations in which the mesh size is also scaled according to the dimensional scaling factors. The stationary tube impacted by a striking mass is simulated using the Lagrangian control-volume method with the clamped un-impacted end restricted in all directions except the z-direction at the impacted end [25]. In order to model materials, 024-PIECEWISE_LINEAR_PLASTICITY is used when the strain-rate effect is considered using the Cowper-Symonds constitutive equation and 098-SIMPLIFIED_JOHNSON_COOK is used, where the strain-rate and strain-hardening effects are taken into account using the Johnson-Cook constitutive equation. The Flanagan-Belytschko stiffness form (i.e. IHQ) with hourglass coefficient of 0.03 (i.e. QM=0.03), which is suitable for impact problems, is used [29]. Moreover, the AUTOMATIC_SURFACE_TO_SURFACE contact model is applied in the simulation procedure and the AUTOMATIC_SINGLE_SURFACE contact model is used to create a contact between the different parts of tube with each other. The static and dynamic friction coefficients are respectively set to be equal to 0.30 and 0.25 in all simulations. A general depiction of axially impacted tube simulated by the LS-Dyna finite element software is shown in Fig. 5.

4.1. Validation of numerical results

Considered is a tube with the thickness, outer diameter and length equal to $2.10\ \mathrm{mm}$, $30.24\ \mathrm{mm}$ and $80\ \mathrm{mm}$, respectively. The stationary tube made of a strain rate insensitive aluminium alloy with properties tabulated at Table 1 is impacted by a striking mass having a mass and velocity equating to $0.26\ \mathrm{kg}$ and $57\ \mathrm{mm/ms}$, respectively. The experimental shortening of the tube is reported equal to $13.80\ \mathrm{mm}$ [25] and it is numerically predicted to be equal to $11.70\ \mathrm{mm}$; thus there is an approximately acceptable agreement between these values (the error percentage is 15.22%). Furthermore, the experimental and numerical buckling shapes are compared with each other according to Fig. 6. It is revealed that both buckling shapes respond to the axial impact by forming a dominant fold at the impacted end. Illustrated by Fig. 6, the experimental and numerical buckling shapes are generally matched. The source of the error observed here between the experimental and numerical result is primarily due to uncertainties in material properties, as a precise material study was not conducted in Ref. [25].

To demonstrate explicitly that improved accuracy is possible with precise material properties consider a stationary tube made out of steel material having thickness, inner diameter and length equal to $1\ \mathrm{mm}$, $26.60\ \mathrm{mm}$ and $60\ \mathrm{mm}$, respectively. The steel tube is axially impacted by a striking mass having respectively the mass and initial velocity equal to $1\ \mathrm{kg}$ and $40\ \mathrm{mm/ms}$ [2]. An element size of $0.25\ \mathrm{mm}$ is selected as this leads to converged results independent of further reduction in element size [2]. The material properties obtained from an experimental study are: Poisson ratio, density, elastic modulus, A, B, n, C and $\dot{\varepsilon}^0$ respectively equal to 0.30, $7864\ \mathrm{kg/m^3}$, $200\ \mathrm{GPa}$, $291.96\ \mathrm{MPa}$, $358.25\ \mathrm{MPa}$, 304.98×10^{-3}, 135.09×10^{-3} and $8.62\times10^{-5}\ \mathrm{1/ms}$ [2]. The reported material properties were determined according to Ref. [2] by conducting static tensile tests using static tensile testing machine and high rate tests using a split Hopkinson pressure bar. The experimental shortening reported equal to $15.20\ \mathrm{mm}$ [2] is predicted equal to $15.40\ \mathrm{mm}$ using the performed numerical simulation, which shows an error equal to 1.32%. Experimental and numerical buckling shapes depicted in Fig. 7 have good agreement with each other. It is revealed that both tubes have a very mild fold at the impacted end, and they also have two folds at the distal end; one of them is a fully formed wrinkle whilst the other is partially formed. Furthermore, the axial force versus time curves at the distal end of the experimentally and numerically impacted tube are provided in Fig. 7 showing an acceptable agreement between them. As illustrated in this figure, the experimental peak load of 73.29 kN is numerically predicted equal to 81.02 kN showing a discrepancy of 10.55%.

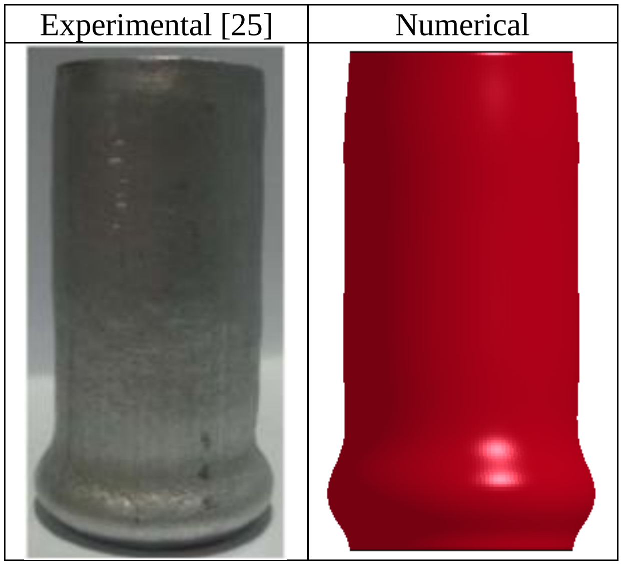

Figure 6. A comparison between the experimental and numerical buckling shapes.

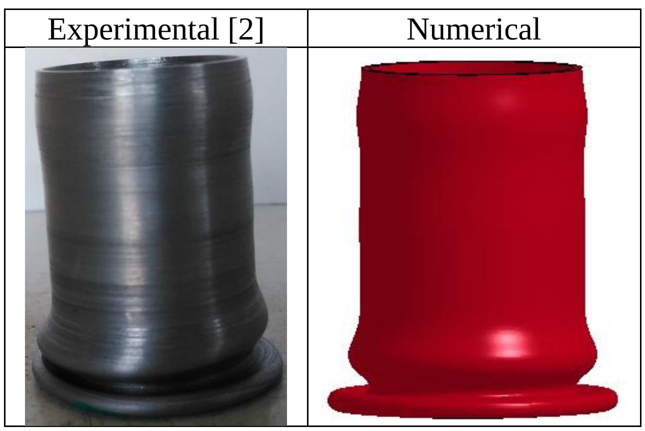

(a) Buckling shapes

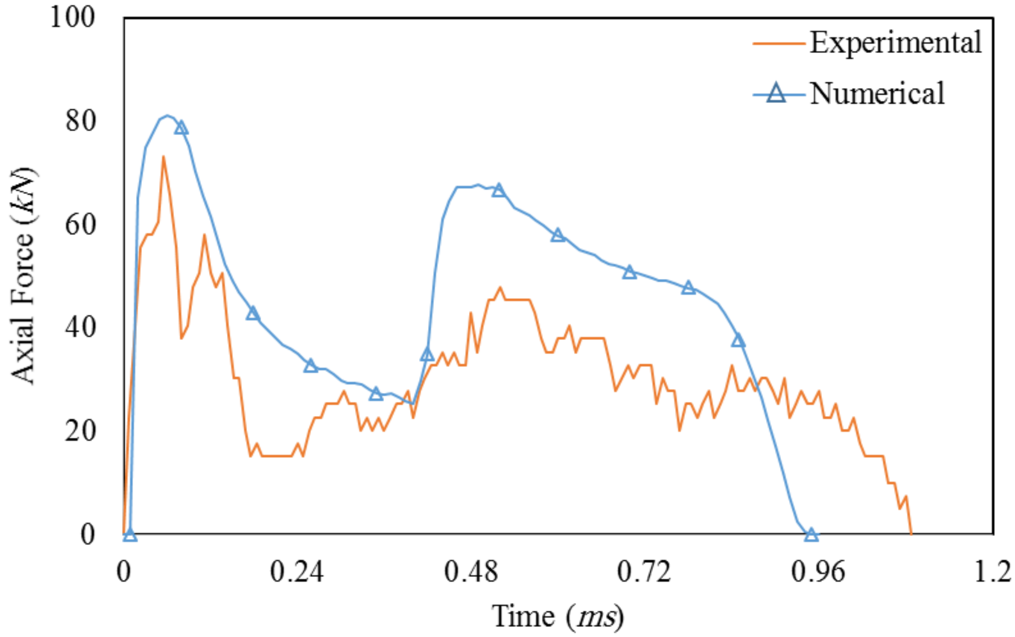

(b) Axial force versus time curves

Figure 7. A comparison between the experimental [2] and numerical buckling shapes and axial force versus time curves.

4.2. Case Study I: Analytical relation (Cowper-Symonds constitutive equation)

In this section, the first-order finite similitude theory is demonstrated by means of an analytical example in which the peak loads of axially impacted tubes are calculated. Firstly, the peak load of axially impacted tubes made of strain rate insensitive materials is predicted. Secondly, the peak load of axially impacted tubes made of strain rate sensitive materials are anticipated.

4.2.1. Case Study I: Analytical relation (strain rate insensitive)

The peak load of a tube subjected to an axial impact can be calculated using an analytical relationship derived based on stress wave propagation, and it is presented in [30-31] as:

$$P_{Peak} = 2\pi RH\left(\frac{2\sigma_0}{\sqrt{3}} + 2v_0\sqrt{\frac{\rho E_h}{3}}\right) \tag{24}$$

where P_{Peak}, R, H, σ_0, v_0, ρ and E_h respectively represent the peak load, mean radius, thickness, initial-yield stress, initial velocity, density and linear strain hardening.

In the following, the presented method based on the first-order finite similitude theory is tested using the analytical relationship (i.e. Eq. (24)). Consider the full-scale and virtual models (see Fig. 4) with properties listed at Tables 2 and 3. Also, the material properties of the full-scale and virtual models are tabulated according to Table 1. It should be emphasized that the presented materials according to Table 1 are inherently strain-rate insensitive. Virtual models 1-6 are designed based on the zeroth-order theory in which an attempt is made cover all possible choices by fixing the initial-yield stress, fixing the linear strain hardening and simultaneous fixing a combination of the initial-yield stress and linear-strain hardening based on the mean value theorem [2, 16, 18] (i.e. the mean value of the rigid stress-strain curve is fixed). Virtual-models 7-9 are designed based on the first-order identities presented in Section 2.4 in which the initial-yield stress and linear strain hardening are simultaneously fixed by solving Eqs. (21) with two different degrees of freedom (i.e. g_1 and g_2). According to the presented peak loads in Table 3, it is clear that the virtual models scaled to half of full size predict the peak load of the full-scale model with non-zero error when the zeroth-order finite similitude theory is used in which the error percentage is considerable for virtual models made of Al 2024. Note that in most practical situations it is not always possible to perform an experiment with a full-scale model, so it can be difficult to anticipate which model will predict to good accuracy the responses of a full-scale model. It is required therefore a method (such as the first order finite-similitude approach) that can automatically predict the responses of the intended models with best accuracy. Based on the presented peak loads in Table 3, it is apparent that the peak load of the full-scale model is predicted with zero error using the first-order finite similitude theory.

Table 1. The material properties of the strain rate insensitive materials.

Material	Yield stress: σ_s (MPa)	Elastic modulus (GPa)	Linear strain hardening: E_h (MPa)	Density (kg/m^3)	Poisson ratio
Al 6061-T6 [25]	310	67.50	1240	2700	0.33
Al 2024-T3 [25]	366	73.10	2800	2780	0.33
Aluminium alloy [25]	140	67	557.62	2700	0.33

Table 2. The properties of the full-scale and virtual models.

Model	Method	Fixed parameters	Material: First trial model	Material: Second trial model	Scaling parameters: β_1	β_2	α_{01}^{ρ}	α_{02}^{ρ}	g_1	g_2	R_1
Full-Scale	-	-	Al 6061	-	-	-	-	-	-	-	-
Virtual Model 1	Zeroth order	σ_s (refer to Eq. (24))	Al 2024	-	0.50	-	7.77	-	0.47	-	-
Virtual Model 2	Zeroth order	σ_s	Al alloy	-	0.50	-	8	-	0.74	-	-
Virtual Model 3	Zeroth order	E_h (refer to Eq. (24))	Al 2024	-	0.50	-	7.77	-	0.34	-	-
Virtual Model 4	Zeroth order	E_h	Al alloy	-	0.50	-	8	-	0.75	-	-
Virtual Model 5	Zeroth order	Mean value (refer to Refs. [2, 16 and 18])	Al 2024	-	0.50	-	7.77	-	0.37	-	-
Virtual Model 6	Zeroth order	Mean value	Al alloy	-	0.50	-	8	-	0.75	-	-
Virtual Model 7	First order	σ_s and E_h (refer to Eq. (24))	Al 2024	Al alloy	0.50	0.35	7.77	23.32	0.33	0.52	-0.99
Virtual Model 8	First order	σ_s and E_h (refer to Eq. (24))	Al 2024	Al alloy	0.50	0.30	7.77	37.04	0.26	0.45	-0.99
Virtual Model 9	First order	σ_s and E_h (refer to Eq. (24))	Al 2024	Al alloy	0.50	0.25	7.77	64	0.30	0.37	-0.99

Table 3. The properties and peak loads of the full-scale and virtual models.

Model	Tube geometrical properties (mm): Thickness, First trial model	Thickness, Second trial model	Mean radius, First trial model	Mean radius, Second trial model	Striking mass velocity (mm/ms): First trial model	Second trial model	Peak load (kN) (Error%)
Full-Scale	2.10	-	14.07	-	120	-	113.52
Virtual Model 1	1.05	-	7.04	-	128.50	-	131.55 (15.88%)
Virtual Model 2	1.05	-	7.04	-	80.64	-	113.42 (0.10%)
Virtual Model 3	1.05	-	7.04	-	177.71	-	81.82 (27.93%)
Virtual Model 4	1.05	-	7.04	-	80.47	-	113.81 (0.26%)
Virtual Model 5	1.05	-	7.04	-	162.97	-	92.65 (18.38%)
Virtual Model 6	1.05	-	7.04	-	80.53	-	113.68 (0.14%)
Virtual Model 7	1.05	0.74	7.04	4.93	182.67	80.45	113.52 (0%)
Virtual Model 8	1.05	0.63	7.04	4.22	233.38	80.21	113.50 (0%)

Virtual Model 9	1.05	0.53	7.04	3.52	197.73	80.39	113.52 (0%)

4.2.2. Case Study I: Analytical relation (Cowper-Symonds constitutive equation)

By considering the strain rate effects using the Cowper-Symonds constitutive equation, the peak load of a tube subjected to an axial impact can be obtained as [30-31]:

$$P_{Peak} = 2\pi RH\left(\frac{2}{\sqrt{3}}\sigma_0\left(1+\left(\frac{\dot{\varepsilon}}{D}\right)^{\frac{1}{q}}\right)+2v_0\sqrt{\frac{\rho}{3}E_h\left(1+\left(\frac{\dot{\varepsilon}}{D}\right)^{\frac{1}{q}}\right)}\right) \tag{25}$$

where $\dot{\varepsilon}$ represents strain rates and D and q are experimentally determined constants. According to Eq. (25), when the strain-rate effects are considered using the Cowper-Symonds constitutive equation, two different degrees of freedom are required to simultaneously fix the initial-yield stress and strain hardening effects. In Eq. (25) the initial-yield stress and the linear strain hardening are two independent physical properties that require two degrees of freedom to scale their effects. In the following, the presented method based on the first-order finite similitude theory is tested using the analytical relation in Eq. (25).

Consider then the full-scale and virtual models with properties listed at Tables 4 and 5. Also, the material properties of the full-scale and virtual models are tabulated according to Table 6. Note that virtual models 1-6 are designed based on the zeroth-order theory in which the developed method in Refs. [2, 16, 18] based on the mean-value theorem is used. It was found in Refs. [2, 16, 18] that the developed method based on the mean-value theorem and the zeroth-order finite similitude theory can provide much better results compared with other methods. In this section, it will be revealed that the developed method in Sections 2.4 and 3 can provide even better results than the method presented in Refs. [2, 16, 18]. Virtual-models 7-20 are designed based on the first-order theory presented in Sections 2.4 and 3 in which the initial-yield stress as function of strain rate and the linear strain hardening as function of strain rates are simultaneously fixed with two different degrees of freedom (i.e. g_1 and g_2) for the first time. According to Tables 4 and 5 and Fig. 8, a comparison is performed for the zeroth-order method in which it is found that fixing the mean value of the initial-yield stress provides much better predictions than fixing of the mean value of the linear strain hardening. In the following, the results of the first-order theory are compared with the best design of the zeroth-order theory (i.e. when the mean value of the initial-yield stress is fixed).

As it mentioned in Section 3, in this exploratory study R_1 is free to be set to any value provided the temporal scaling parameters g_1 and g_2 are reasonable. A zero R_1 value returns zeroth-order identities, so a reasonable initial exploratory range for R_1 might be $-1 < R_1 < 1$, where it is appreciated that R_1 can take up negative or positive values. Note that R_1 provides a measure of how far the identities in Eqs. (12) depart from zeroth-order behaviour with scale. The fact that the theory provides only one single parameter R_1 for all the physical quantities in Eq. (12) is an impressive aspect of the theory. In the trials presented here the range $-1 < R_1 \leq 0$ provides positive real values for g_1 and g_2 on solution of Eqs. (21). This feature is revealed in Tables 4 and 5 and Fig. 9, where the effect of R_1 over the critical range $-1 < R_1 \leq 0$ and beyond (i.e. $1 \leq |R_1| \leq 1000$) is investigated for virtual model 9. Note that, results for the range $1 \leq |R_1| \leq 1000$ are presented in Table 4 to largely confirm the expected outcome that no useful information is obtained, as revealed by g_1 and g_2 taking on complex values. Note that although accuracy of the first-order theory is affected by the values of R_1, it always predicts the peak load of the full-scale model with greater accuracy than the zeroth-order theory.

Also, the peak load of full-scale model is predicted using the methods developed based on the zeroth-order and first-order theories according to Figs. 10 and 11 in which the effects of materials and dimensional scaling factors of the second projected models are sought. It is revealed that the peak load of full-scale model is not considerably affected by the dimensional scaling factors of the second projected models. Also, it is found that the peak load of full-scale model is predicted to good accuracy using the method derived based on the first-order theory for all the used materials. Furthermore, it is revealed that the first-order finite similitude theory predicts the response of full-scale model with greater accuracy than the zeroth-order theory. It should be emphasized that the reported errors in the depicted figures are calculated based on the areas under the curves.

Finally, the effect of small dimensional scaling factors (e.g. $\beta_2 = 0.008$) on accuracy is presented in Fig. 12. The figure confirms that prediction accuracy with the first-order theory is not significantly diminished by large reductions in scale. Up to a 125-fold reduction is presented in

Fig. 12 but similar to the studies above, for peak load versus different strain rate, predictions are returned with errors close to zero.

Table 4. The properties of the full-scale and virtual models.

Model	Method	Fixed parameters	Material		Scaling parameters						
			First trial model	Second trial model	β_1	β_2	α_{01}^{ρ}	α_{02}^{ρ}	g_1	g_2	R_1
Full-Scale	-	-	Magnesium	-	-	-	-	-	-	-	-
Virtual Model 1	Zeroth order	$\bar{Y}$ (refer to Eq. (17a))	Steel	-	0.50	-	1.73	-	0.73	-	-
Virtual Model 2		$\bar{H}^{*}$ (refer to Eq. (17b))	Steel	-	0.50	-	1.73	-	0.40	-	-
Virtual Model 3		$\bar{Y}$	Aluminium	-	0.50	-	5.07	-	0.57	-	-
Virtual Model 4		$\bar{H}$	Aluminium	-	0.50	-	5.07	-	0.87	-	-
Virtual Model 5		$\bar{Y}$	Copper	-	0.50	-	1.52	-	0.95	-	-
Virtual Model 6		$\bar{H}$	Copper	-	0.50	-	1.52	-	1.96	-	-
Virtual Model 7	First order	$\bar{Y}$ and $\bar{H}$ (refer to Eqs. (17))	Steel	Aluminium	0.50	0.45	1.73	6.95	0.37	0.94	-0.24
Virtual Model 8					0.50	0.40	1.73	9.89	0.50	0.53	-0.58
Virtual Model 9					0.50	0.30	1.73	23.45	No solution or complex values		1000
					0.50	0.30	1.73	23.45			100
					0.50	0.30	1.73	23.45			10
					0.50	0.30	1.73	23.45			5
					0.50	0.30	1.73	23.45			1
					0.50	0.30	1.73	23.45	0.34	0.98	-0.10
					0.50	0.30	1.73	23.45	0.38	0.56	-0.30
					0.50	0.30	1.73	23.45	0.46	0.43	-0.50
					0.50	0.30	1.73	23.45	0.60	0.36	-0.70
					0.50	0.30	1.73	23.45	1.08	0.32	-0.90
					0.50	0.30	1.73	23.45	No solution or complex values		-2
					0.50	0.30	1.73	23.45			-5
					0.50	0.30	1.73	23.45			-10
					0.50	0.30	1.73	23.45			-100
					0.50	0.30	1.73	23.45			-1000
Virtual Model 10					0.50	0.20	1.73	79.14	0.35	0.48	-0.18
Virtual Model 11					0.50	0.10	1.73	633.15	0.35	0.23	-0.18
Virtual Model 12			Steel	Copper	0.50	0.45	1.73	2.09	0.42	1.45	-0.27
Virtual Model 13					0.50	0.40	1.73	2.98	0.39	1.66	-0.17
Virtual Model 14					0.50	0.30	1.73	7.05	0.38	1.66	-0.09

Virtual Model 15					0.50	0.20	1.73	23.80	0.38	0.95	-0.12
Virtual Model 16					0.50	0.10	1.73	190.37	0.37	0.68	-0.06
Virtual Model 17					0.02	1.33×10^{-2}	2.71×10^{4}	8.03×10^{4}	0.01	0.04	-0.20
Virtual Model 18					0.02	0.01	2.71×10^{4}	1.90×10^{5}	0.01	0.04	-0.15
Virtual Model 19					1.33×10^{-2}	0.01	9.14×10^{4}	1.90×10^{5}	0.01	0.03	-0.20
Virtual Model 20					0.01	0.80×10^{-2}	2.17×10^{5}	3.72×10^{5}	0.01	0.03	-0.16

*In this section, $\bar{H}$ refers to the mean value of linear strain hardening as a function of strain rate (i.e. the mean value of the identity $E_h\left(1+\left(\dot{\varepsilon}/D\right)^{1/q}\right)$)

Table 5. The properties of the full-scale and virtual models.

Model	Tube geometrical properties (mm)						Striking mass			
	Thickness		Mean radius		Length		Velocity (mm/ms)		Mass (kg)	
	First trial model	Second trial model	First trial model	Second trial model	First trial model	Second trial model	First trial model	Second trial model	First trial model	Second trial model
Full-Scale	2.10	-	14.07	-	80	-	120	-	0.26	-
Virtual Model 1	1.05	-	7.04	-	40	-	82.36	-	0.15	-
Virtual Model 2	1.05	-	7.04	-	40	-	150.99	-	0.15	-
Virtual Model 3	1.05	-	7.04	-	40	-	105.18	-	0.05	-
Virtual Model 4	1.05	-	7.04	-	40	-	68.87	-	0.05	-
Virtual Model 5	1.05	-	7.04	-	40	-	62.98	-	0.17	-
Virtual Model 6	1.05	-	7.04	-	40	-	30.60	-	0.17	-
Virtual Model 7	1.05	0.95	7.04	6.33	40	36	163.70	57.20	0.15	0.04
Virtual Model 8	1.05	0.84	7.04	5.63	40	32	119.54	90.09	0.15	0.03
Virtual Model 9 9/1	1.05	0.63	7.04	4.22	40	24	179.20	36.93	0.15	0.01
Virtual Model 9 9/2	1.05	0.63	7.04	4.22			156.59	64.88		
Virtual Model 9 9/3	1.05	0.63	7.04	4.22			130.76	84.38		
Virtual Model 9 9/4	1.05	0.63	7.04	4.22			99.50	100.34		
Virtual Model 9 9/5	1.05	0.63	7.04	4.22			55.42	114.21		
Virtual Model 10	1.05	0.42	7.04	2.81	40	16	170.65	50.23	0.15	3.30×10^{-3}
Virtual Model 11	1.05	0.21	7.04	1.41	40	8	170.42	51.62	0.15	4.11×10^{-4}
Virtual Model 12	1.05	0.95	7.04	6.33	40	36	142.64	37.23	0.15	0.13

Virtual Model 13	1.05	0.84	7.04	5.63	40	32	153.31	28.88	0.15	0.09
Virtual Model 14	1.05	0.63	7.04	4.22	40	24	160.21	21.74	0.15	0.04
Virtual Model 15	1.05	0.42	7.04	2.81	40	16	157.67	25.39	0.15	0.01
Virtual Model 16	1.05	0.21	7.04	1.41	40	8	163.77	17.56	0.15	1.37×10^{-3}
Virtual Model 17	4.20×10^{-2}	2.80×10^{-2}	28.14×10^{-2}	18.76×10^{-2}	1.60	1.07	198.93	39.82	9.59×10^{-6}	3.24×10^{-6}
Virtual Model 18	4.20×10^{-2}	2.10×10^{-2}	28.14×10^{-2}	14.07×10^{-2}	1.60	0.80	206.22	34.34	9.59×10^{-6}	1.37×10^{-6}
Virtual Model 19	2.80×10^{-2}	2.10×10^{-2}	18.76×10^{-2}	14.07×10^{-2}	1.07	0.80	208.08	40.30	2.85×10^{-6}	1.37×10^{-6}
Virtual Model 20	2.10×10^{-2}	1.68×10^{-2}	14.07×10^{-2}	11.26×10^{-2}	0.80	0.64	220.59	36.16	1.20×10^{-6}	6.99×10^{-7}

Table 6. The material properties of the strain rate sensitive materials.

Material	Yield stress: σ_s (MPa)	Elastic modulus (GPa)	Linear strain hardening: E_h (MPa)	Density (kg/m^3)	Poisson ratio $\times 10^{-1}$	D ($1/ms$) $\times 10^{-2}$	q
AZ31B-H24 magnesium [32]	197.40	45.00	828.60	1700	2.90	2412.49	3.09
Steel [33]	345.00	210.00	4500.00	7850	2.86	684.40	3.91
Aluminium [30]	295.00	72.40	542.60	2685	3.30	128800.00	4.00
Copper [34]	204.60	123.60	218.76	8930	3.40	177.80	4.99

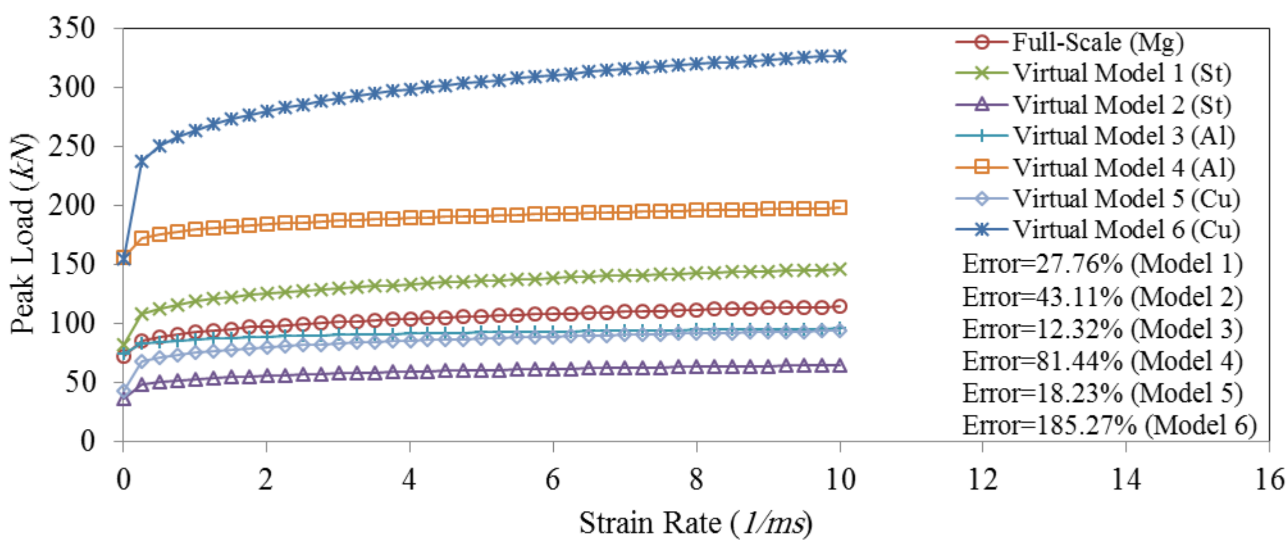

Figure 8. A comparison between the zeroth order methods.

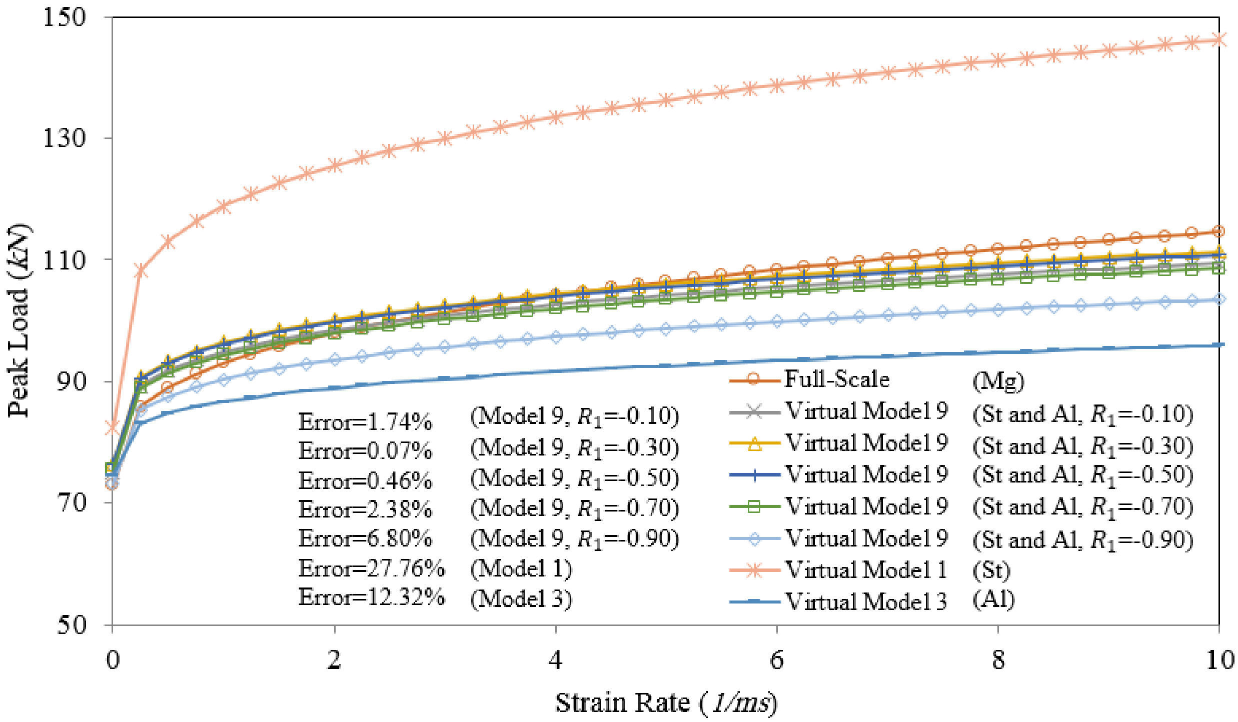

Figure 9. An investigation into the effect of R_1 values on the results.

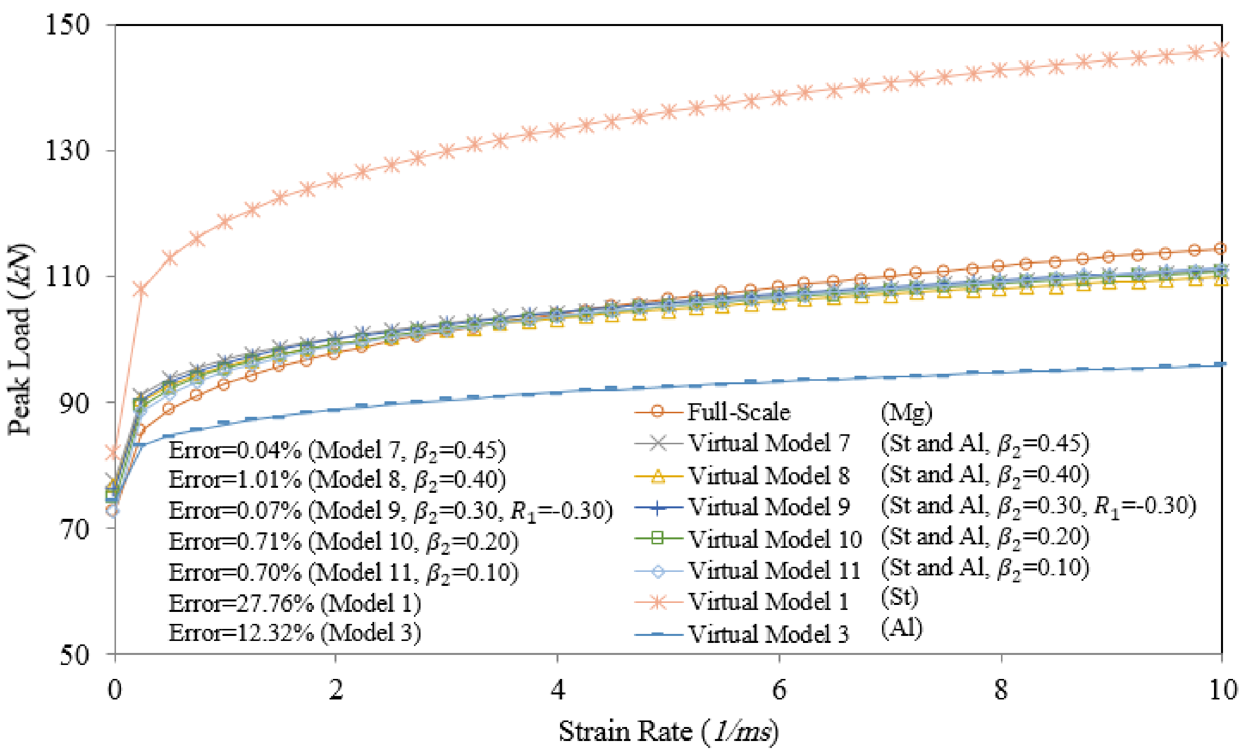

Figure 10. An investigation into the effect of the second dimensional scaling factors and the different materials on the results.

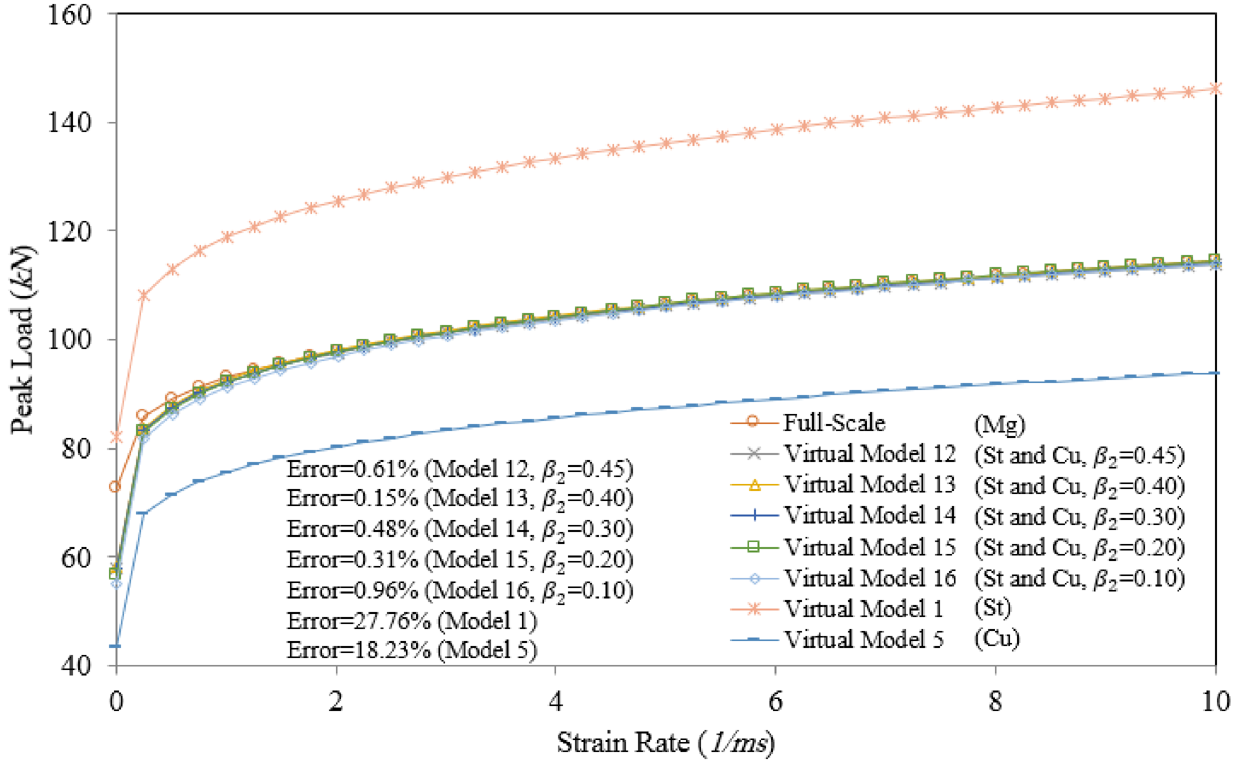

Figure 11. An investigation into the effect of the second dimensional scaling factors and the different materials on the results.

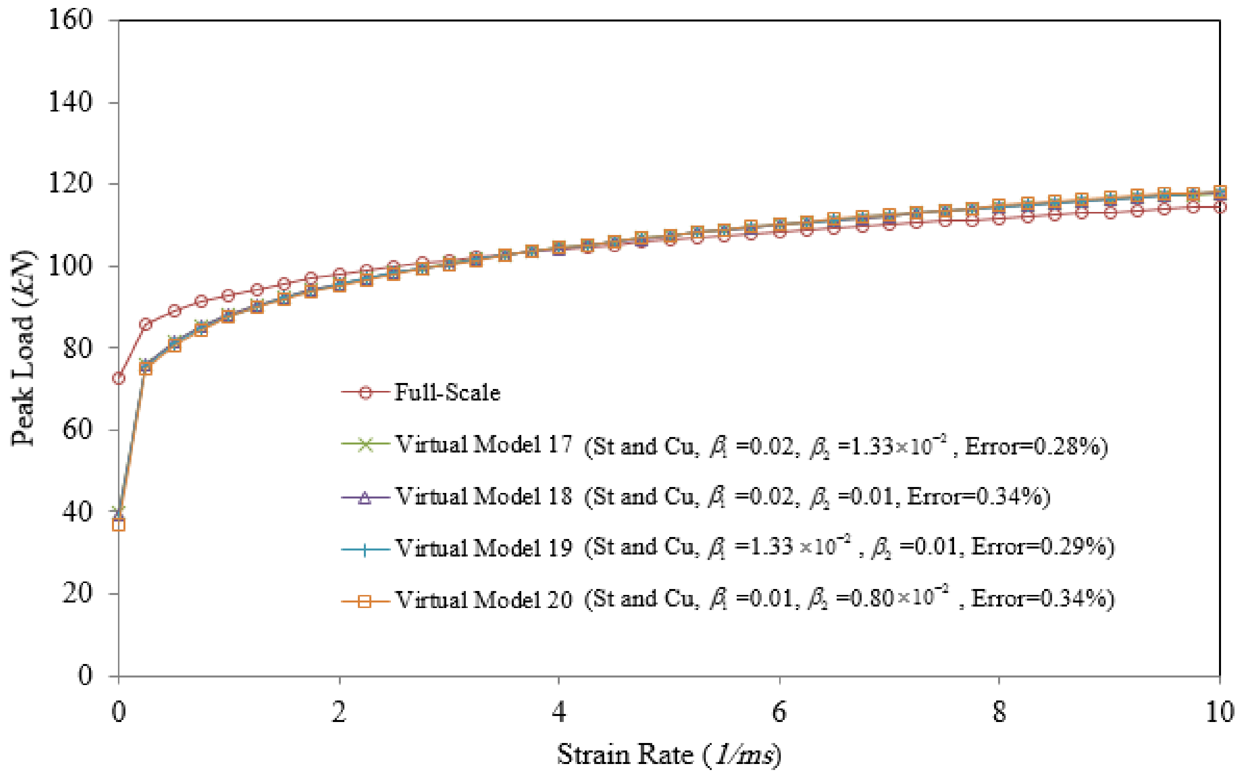

Figure 12. An investigation into the effect of the large dimensional scaling factors on the accuracy of predictions.

4.3. Case Study II: Numerical results (Cowper-Symonds constitutive equation)

Considered here are the full-scale and virtual models with properties listed in Tables 4 and 5. Furthermore, the material properties of the full-scale and virtual models are tabulated according to Table 6. The virtual-models 1, 3 and 5 are designed based on the zeroth order theory in which the developed method in Refs. [2, 16, 18] based on a mean-value theorem is used. The full-scale and virtual-models 1, 3 and 5 are respectively made of magnesium, steel, aluminium and copper materials presented at Table 6; also, virtual-models 1, 3 and 5 are scaled to half of the full-size dimensions. Plus, virtual-models 9/2 and 14, which are designed based on the first-order theory, are presented according to Tables 4 and 5. Virtual-models 9/2 and 14 are formed from two different models and are designed to improve the accuracy of the predictions provided by virtual-model 1 made of steel material. In other words, an attempt is made to use the first-order theory to enhance the predictions provided by virtual-model 1 by using virtual-models 3 and 5, which are respectively made of aluminium and copper. As recorded in Tables 4 and 5, virtual-model 9/2 is formed from two models: the first one is scaled to 0.50 and made of steel; and the second one is scaled to 0.30

and made of aluminium. Similarly, it is revealed that virtual-model 14 is formed from two models: the first one is scaled to 0.50 and made of steel; and the second one is scaled to 0.30 and made of copper. Also, virtual-models 9/2 and 14 are designed based on the first-order theory in which the mean value of the initial-yield stress and the mean value of the linear strain hardening are simultaneously fixed, whilst virtual-models 1, 3 and 5 are designed based on the zeroth-order theory in which only one feature of the stress-strain curve is fixed, i.e. the mean value of the initial-yield stress.

The axial force-time, shortening curves and the peak loads together with error percentages of the full-scale and virtual models 1, 3, 5, 9/2 and 14, presented in Tables 4 and 5, are respectively presented according to Fig. 13 and Table 7. Also, the buckling shapes, the shortenings and the maximum outside radius together with error percentages of the full-scale and virtual models 1, 3, 5, 9/2 and 14 are presented according to Fig. 14 and Table 7. The depicted errors in Fig. 13 are calculated based on the area under the curves.

According to Fig. 13 and Table 7, it is clear that virtual-models 3 and 5 designed based on the zeroth-order theory and respectively made of aluminium and copper materials predict the response of the full-scale model to a good accuracy whereas virtual-model 1 designed based on the zeroth-order theory and made of steel material provides a prediction of the full-scale model structure response with a huge difference since strain hardening is not captured. The unusual response of virtual model 1 in Fig. 13 is mainly due to the relatively high values of the linear strain hardening and yield stress as tabulated in Table 6. An attempt was made to improve the response of virtual-model 1 using models 3 and 5 and the first-order theory. Based on the presented results according to Fig. 13 and Table 7, the responses of the full-scale model are predicted using virtual-models 9/2 and 14 in which a combination of model 1 made of steel with models 3 and 5 made of aluminium and copper materials is used. For example, it is found that the error percentage of 103.33% in predicting the peak load of the full-scale model is respectively decreased to 3.06% and 3.02% when virtual-models 9/2 and 14 are used.

Also, the buckling shapes, the shortenings together with error percentages and the maximum outer-tube radii together with error percentages of the full-scale and virtual models are presented in Fig. 14 and Table 7. It is revealed that virtual-scale model 1, in contrast to the virtual-models 3 and 5, is not able to predict the response of the full-scale model with a good accuracy. However, the accuracy of virtual-model 1 made of steel is enhanced using the first-order theory and models 3 and 5 according to Table 7. Note that the error percentage of 38.51% in predicting the full-scale shortening is respectively decreased to 13.36% and 33.51% when virtual-models 9/2 and 14 are used. Furthermore, the error percentage of 16.75% in predicting the maximum outer full-scale tube radius is decreased to 3.55% and 1.57% when virtual-models 9/2 and 14 are respectively applied. The buckling shapes of virtual models 1, 3 and 5, which are depicted in Fig. 14 (and designed based on the zeroth-order theory) can be directly compared to the full-scale model. However, as depicted in Fig.14, buckling shapes from the individual scaled experiments of the first-order models are required to be combined according to the displacement identity Eq. (23d), which is a facility not available to the Abaqus software.

Table 7. The global outputs of tubes including the peak loads, shortenings and maximum outer tube radius

Case study	Model	The peak loads (kN) (error%)	The shortenings (mm) (error%)	The maximum outer tube radius (mm) (error%)
II	Full-Scale	87.65	24.02	21.67
	Virtual Model 1	178.22 (103.33%)	14.77 (38.51%)	18.04 (16.75%)
	Virtual Model 3	86.53 (1.28%)	29.65 (23.44%)	21.74 (0.32%)
	Virtual Model 5	88.67 (1.16%)	35.30 (46.96%)	21.88 (0.97%)
	Virtual Model 9/2	90.33 (3.06%)	27.23 (13.36%)	20.90 (3.55%)
	Virtual Model 14	85.00 (3.02%)	32.07 (33.51%)	21.33 (1.57%)
III	Full-Scale	72.79	32.60	21.65
	Virtual Model 1	95.45 (31.13%)	27.56 (15.46%)	21.86 (0.97%)
	Virtual Model 2	83.07 (14.12%)	29.58 (9.26%)	21.64 (0.05%)
	Virtual Model 3	81.53 (12.01%)	28.28 (13.25%)	21.94 (1.34%)
	Virtual Model 4	80.69 (10.85%)	29.18 (10.49%)	21.70 (0.23%)
	Virtual Model 5	90.45 (24.26%)	27.38 (16.01%)	21.89 (1.11%)

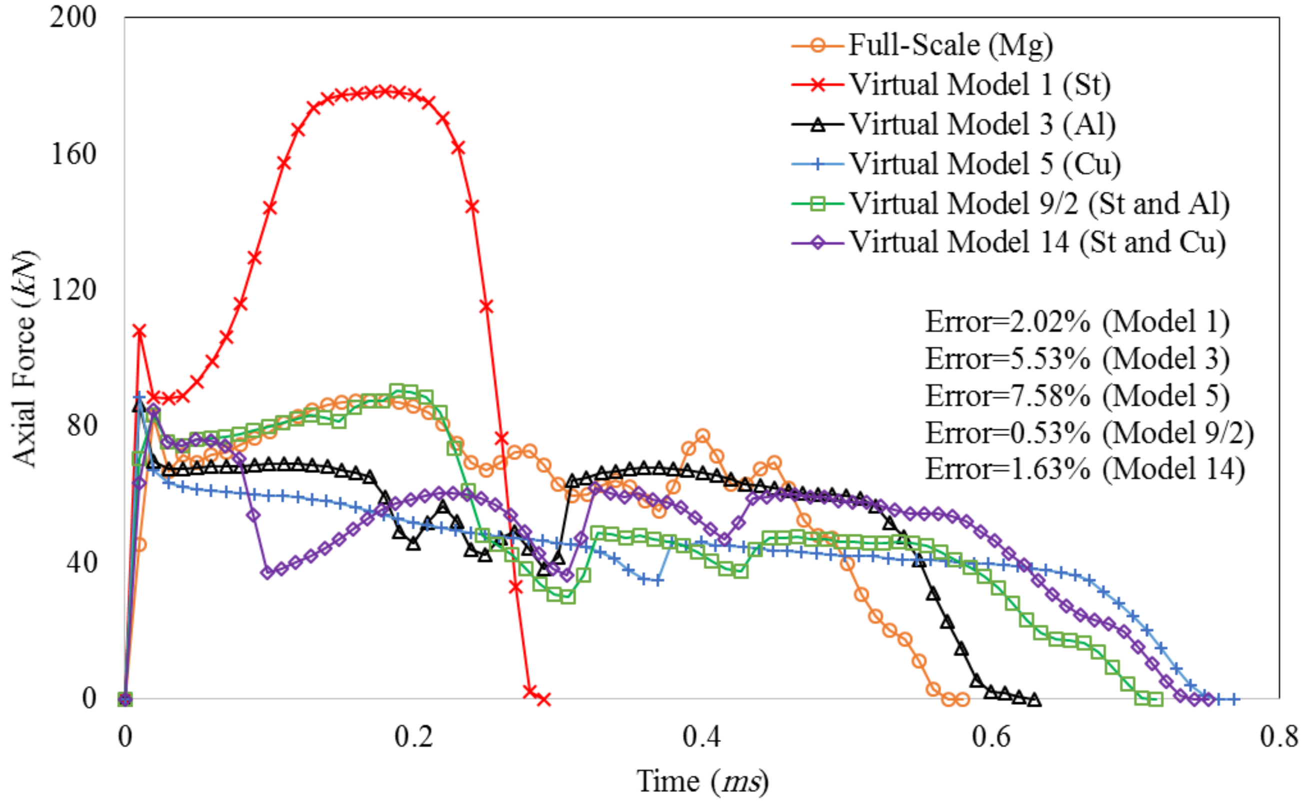

635
636 (a) The axial force versus time curves

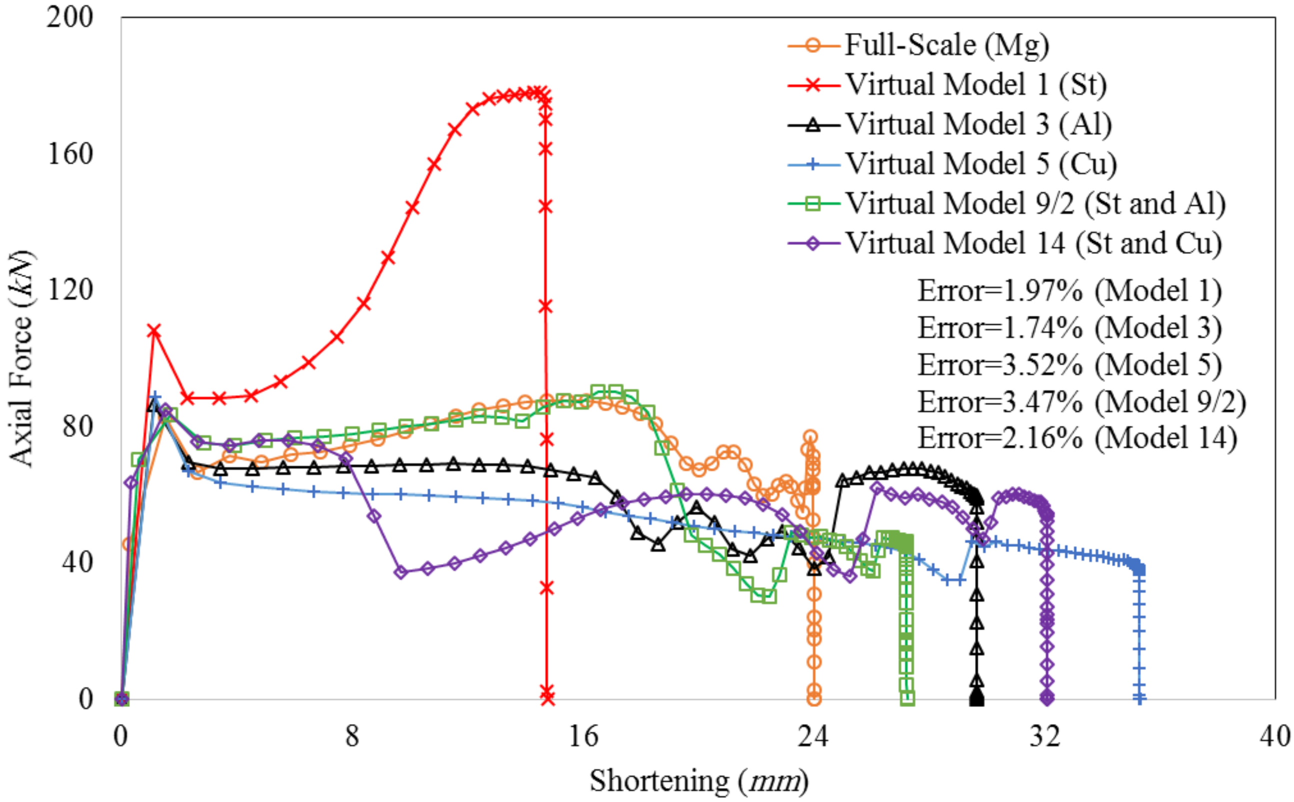

(b) The axial force versus shortening curves

Figure 13. Axial force-time and axial force-shortening curves of full-scale and virtual models.

Full-Scale (Mg)	Zeroth Order Theory Model 1 (St)	Zeroth Order Theory Model 3 (Al)	Zeroth Order Theory Model 5 (Cu)
			

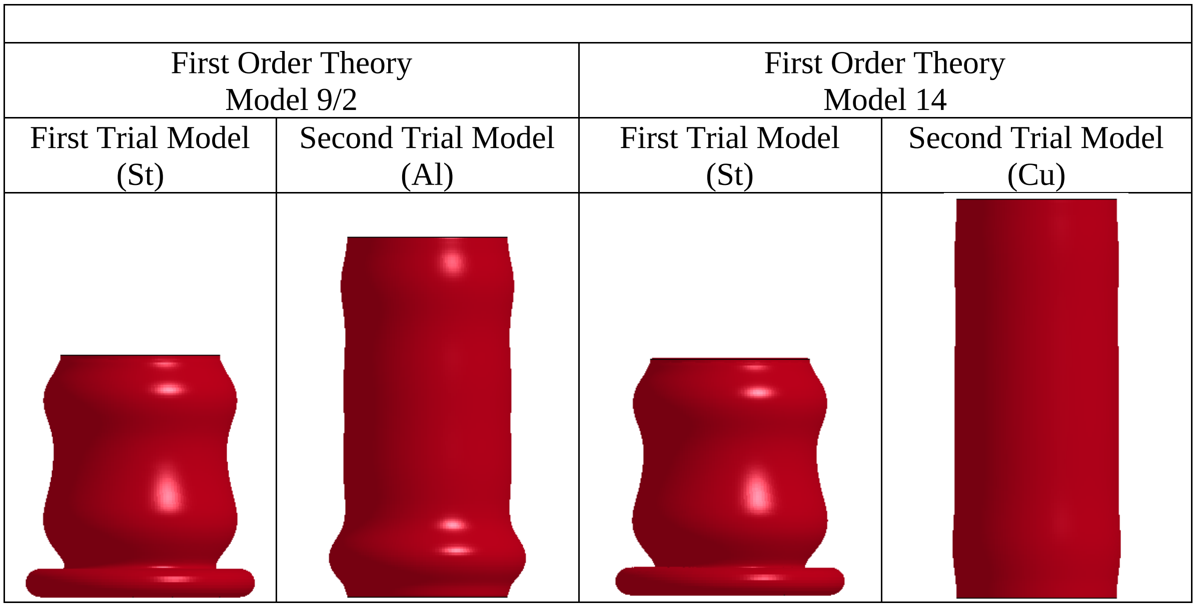

Figure 14. Buckling shapes.

4.4. Case Study III: Numerical results (Johnson-Cook constitutive equation)

The properties of the full-scale and virtual models are tabulated according to Tables 8 and 9. Also, the material properties of the full-scale and virtual models are listed in Table 10. Note here that the Johnson-Cook constitutive equation, which can capture the effects of both the initial-yield stress and strain hardening, is used. Moreover, the best predictions of the intended models are provided in Refs. [2, 16, 18] with the Johnson-Cook constitutive equation employed in zeroth-order scaling. Here it is aimed to show that first-order theory can provide better predictions than those presented in Refs. [2, 16, 18] in which the Johnson-Cook constitutive equation is used. Virtual-models 4 and 5 are designed based on the first-order theory in which Eqs. (21) are employed to determine g_1 and g_2 with R_1 specified. Virtual-models 1-3 are designed based on the zeroth-order theory in which the mean value of the initial-yield stress and strain hardening as function of strain rates is fixed. The full-scale and virtual-models 1-3 are respectively made of magnesium, steel, aluminium and copper materials presented at Table 10. In addition, virtual-models 1-3 are scaled to half of the full-scale dimensions. Plus, virtual-models 4 and 5 are formed from two different models, which are designed to improve the accuracy of the predictions provided by virtual-model 1 made of steel. Thus, the first-order theory is applied here in an attempt to enhance the predictions provided by virtual-model 1 by involving models 2 and 3, which are respectively made of aluminium and copper. As recorded in Tables 8 and 9, virtual-model 4 is formed from models made of steel and aluminium and scaled to 0.50 and 0.30 of the full-scale dimensions. In addition, virtual-model 5 is formed from models, which are respectively made of steel and copper and scaled to 0.50 and 0.30 of the full-scale dimensions.

The axial force-time, shortening curves and the peak loads together with error percentages of the full-scale and virtual-models 1-5, presented in Tables 8 and 9, are respectively presented according to Fig. 15 and Table 7. The depicted errors in Fig. 15 are calculated based on the area under the curves. Also, the buckling shapes, the shortenings and the maximum outer radii together with error percentages of the full-scale and virtual-models 1-5 are presented according to Fig. 16 and Table 7. The buckling shapes provided with the first order theory (i.e. models 4 and 5) are depicted in Fig. 16 and show a reasonable agreement with the full-scale model. Although as mentioned above Abaqus does not have the means to combine the buckling shapes from the individual scaled experiments but by means of Eq. (23) and by identification of the nodes located on the outside surfaces of the tubes the buckling shapes are generated in the graph in Fig. 16 and reasonable replication is revealed.

According to Fig. 15 and Table 7, it is clear that virtual-models 1, 2 and 3 designed based on the zeroth-order theory and respectively made of steel, aluminium and copper materials mostly predict the response of the full-scale model with reasonable accuracy. However, these models do predict some of the full-scale model responses with some error; for example, virtual-model 1 predicts the peak load of the full-scale tube with an error percentage of 31.13%. This is improved using the first-order theory involving models 2 and 3. Virtual-models 4 and 5, based on the first-order theory, reduce the error percentage of 31.13% in prediction of peak load to respectively 10.85% and 24.26%. In all cases, virtual-models 4 and 5 provide improved accuracy over model 1 but errors nevertheless remain.

The buckling shapes, the shortenings together with error percentages and the maximum outer-tube radii together with error percentages of the full-scale and virtual-models 1-5 are presented in Fig. 16 and Table 7. The maximum outer full-scale tube radius is predicted by virtual-models 1-3 (zeroth order) and virtual-models 4-5 (first-order) to good accuracy. However, the shortening of the full-scale model predicted with an error percentage of 15.46% using virtual-model 1 is predicted with an error percentage of 10.49% using virtual-model 4 thus displaying an enhancement in the accuracy of the prediction provided by virtual-model 1.

Finally, it is clear from the results presented in this paper that the new approach predicts the overall responses of impacted tubes such as shortenings, peak loads and even the overall behaviour of the axial force-shortening curves to a good accuracy. However, not insignificant differences can occur at specific points and times, such as those revealed at distinct instances in the axial force-shortening curves (see Fig. 13). Possible sources of improvement are alternative material models and/or application of a higher order finite similitude approach, as this provides additional degrees of freedom, but is an aspect for future study. Additional sources of uncertainly are friction coefficients, which are assumed equal here for full-scale and trial models.

Table 8. The properties of the full-scale and virtual models.

Model	Method	Fixed parameters	Material		Scaling parameters						
			First trial model	Second trial model	β_1	β_2	α_{01}^{ρ}	α_{02}^{ρ}	g_1	g_2	R_1
Full-Scale	-	-	Magnesium	-	-	-	-	-	-	-	-
Virtual Model 1	Zeroth order	$\bar{H}$ (refer to Eq. (17b))	Steel	-	0.50	-	1.80	-	0.91	-	-
Virtual Model 2		$\bar{H}$	Aluminium	-	0.50	-	5.24	-	0.53	-	-
Virtual Model 3		$\bar{H}$	Copper	-	0.50	-	1.58	-	1.28	-	-
Virtual Model 4	First order	$\bar{Y}$ and $\bar{H}$ (refer to Eqs. (17))	Steel	Aluminium	0.50	0.30	1.80	24.28	1.00	0.30	-0.75
Virtual Model 5		$\bar{Y}$ and $\bar{H}$	Steel	Copper	0.50	0.30	1.80	7.32	0.91	0.76	-0.36

Table 9. The properties of the full-scale and virtual models.

Model	Tube geometrical properties (mm)						Striking mass			
	Thickness		Mean radius		Length		Velocity (mm/ms)		Mass (kg)	
	First model	Second model	First model	Second model	First model	Second model	First model	Second model	First model	Second model
Full-Scale	2.10	-	14.07	-	80	-	120	-	0.26	-
Virtual Model 1	1.05	-	7.04	-	40	-	66.09	-	0.15	-
Virtual Model 2	1.05	-	7.04	-	40	-	113.59	-	0.05	-
Virtual Model 3	1.05	-	7.04	-	40	-	47.00	-	0.17	-
Virtual Model 4	1.05	0.63	7.04	4.22	40	24	59.74	118.46	0.15	0.01
Virtual Model 5	1.05	0.63	7.04	4.22	40	24	66.06	47.28	0.15	0.04

Table 10. The material properties.

Material	Density (kg/m^3)	Elastic modulus (GPa)	Poisson ratio $\times 10^{-1}$	A (MPa)	B (MPa)	n $\times 10^{-1}$	C $\times 10^{-1}$	$\dot{\varepsilon}_0$ ($1/ms$) $\times 10^{-3}$
Magnesium [11]	1770	45.00	2.90	224.00	380.00	7.61	0.12	1
Steel [11]	7890	200.00	3.00	350.00	275.00	3.60	0.22	1
Aluminium [11]	2700	72.40	0.33	265	426	3.40	0.15	1
Copper [11]	8960	120.00	3.40	90.00	292.00	3.10	0.25	1

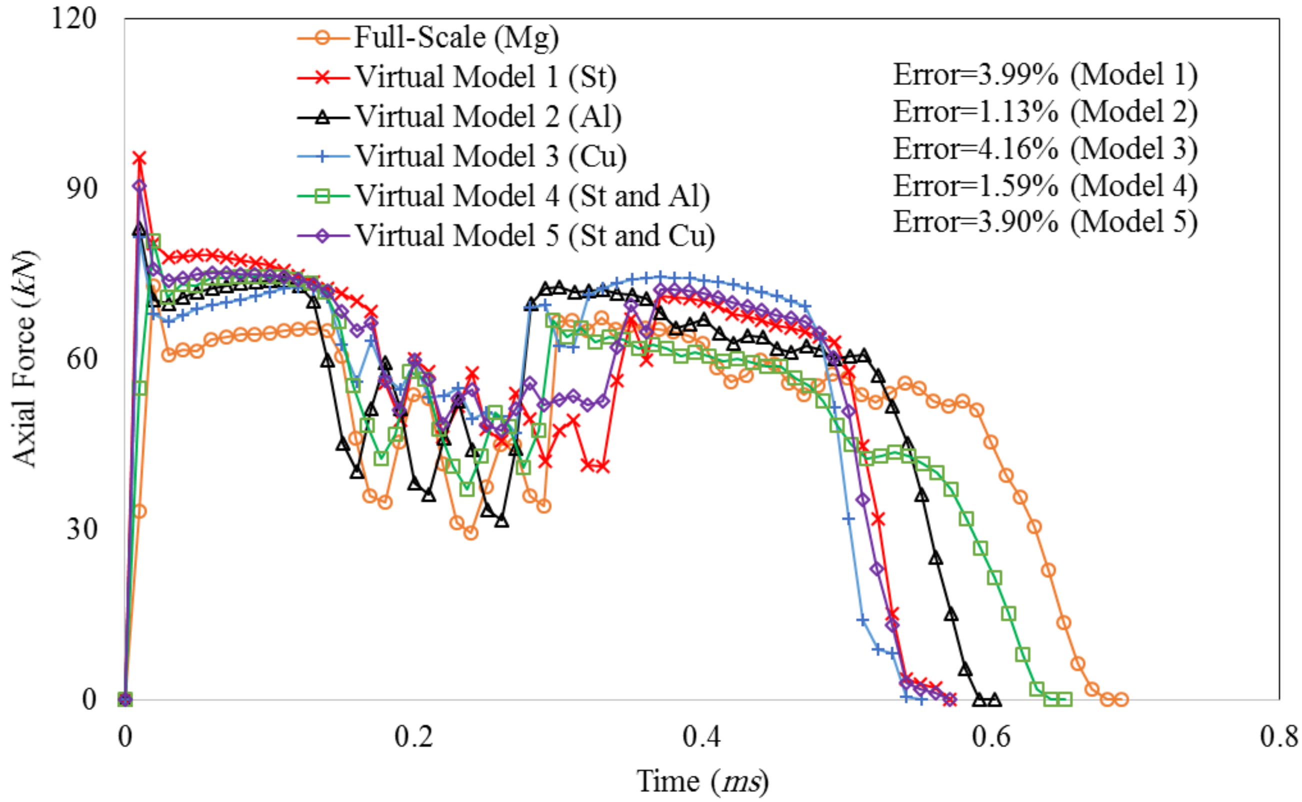

(a) The axial force versus time curves

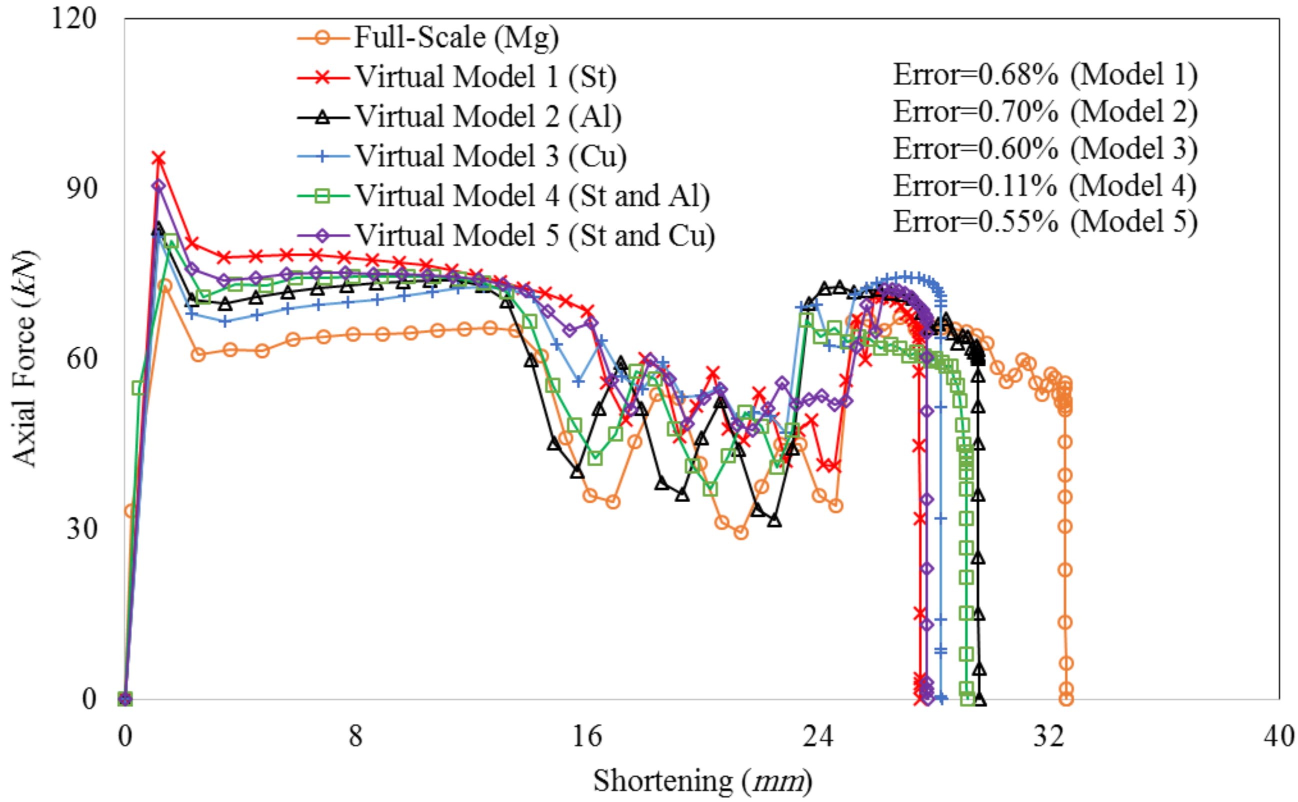

(b) The axial force versus shortening curves

Figure 15. The axial force-time and axial force-shortening curves of full-scale and virtual models.

Full-Scale (Mg)	Zeroth Order Theory Model 1 (St)	Zeroth Order Theory Model 2 (Al)	Zeroth Order Theory Model 3 (Cu)
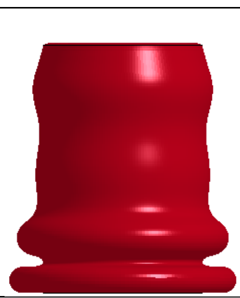			

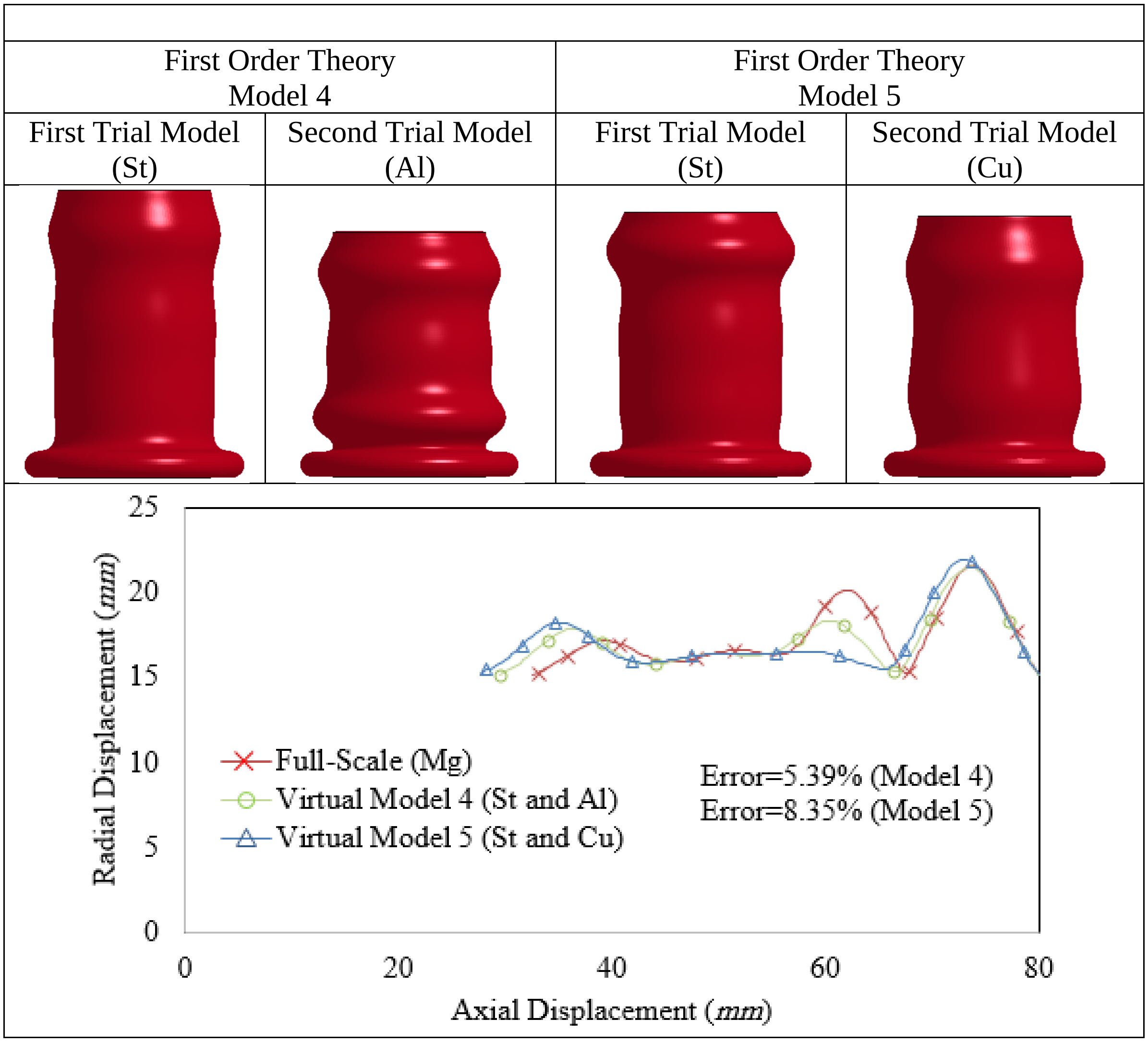

Figure 16. The buckling shapes.

Conclusion

In this paper a method has been developed for scaling of impact processes based on the first-order finite-similitude theory in which response characteristics of full-scale models can be predicted using scaled-trial models at two distinct scales. Adjustment to the initial conditions in the scaled-trial models (e.g. striking velocity and mass) were made to ensure good representations could be made of the behaviour at full scale. The accuracy of both first and zeroth-order finite similitude theories were assessed using both analytical methods and numerical simulations to demonstrate the improvements possible with the new theory.

The following conclusions can be drawn from the work presented in the paper:

- The finite-similitude theory has been further developed to capture all scale dependencies that arise in the fields describing impact mechanics.
- A new differential form of similitude has been established, which when integrated links information across two scaled-impact experiments to the full-scale response.
- Scale effects as previously defined by dimensional analysis cease to be scale effects, since proportional field differences feature in the new theory.
- The new theory is equally applicable to analytical and numerical impact models and overall provides improved accuracy, to that obtained from a single impact scaled experiment.

More specifically for the trial simulation performed it has been show that:

- For first time, the initial-yield stress and linear strain hardening of an impacted structure made of a strain-rate insensitive material were simultaneously targeted using two different scaling parameters. In particular the mean values of initial-yield stress and linear strain hardening were matched for virtual and full-scale models. Comparison with the proposed method based on the zeroth-order theory revealed that an error of 18.38% in peak load estimated by a strain rate insensitive analytical model (Eq. (24)) can be decreased to 0% when the new method is used.
- In numerical simulations in which the Cowper-Symonds constitutive equation was used, an error of 103.33% in predicting peak load with a single trial-steel tube was decreased to 3.06% and 3.02% when respectively combined with the trial models made of aluminium and copper.
- In numerical simulations in which the Johnson-Cook constitutive equation was used, an error of 31.13% in prediction of peak load created by a trial model made of steel was decreased to 10.85% when combined with a trial model made of aluminium using the first-order theory.

Acknowledgements

No funding body was involved in the production of this work.

References

[1] Oshiro RE, Alves M. Scaling Impacted Structures. Archive of Applied Mechanics 2004;74:130-145.

[2] Sadeghi H, Davey K, Darvizeh R, Rajabiehfard R, Darvizeh A. An Investigation into Finite Similitude for High-Rate Loading Processes: Advantages in Comparison to Dimensional Analysis and Its Practical Implementation. International Journal of Impact Engineering 2020;140:103554.

[3] Jones N. Structural Impact. 2nd ed. Cambridge: Cambridge University Press; 2012.

[4] Booth E, Collier D, Miles J. Impact Scalability of Plated Steel Structures. In: Jones N, Wierzbicki T, editors. Structural Crashworthiness. London: Butterworths; 1983;136-174.

[5] Jiang P, Tian CJ, Xie RZ, Meng DS. Experimental Investigation into Scaling Laws for Conical Shells Struck by Projectiles. International Journal of Impact Engineering 2006;32:1284-1298.

[6] Alves M, Oshiro RE. Scaling the Impact of a Mass on a Structure. International Journal of Impact Engineering 2006;32:1158-1173.

[7] Oshiro RE, Alves M. Scaling of Cylindrical Shells under Axial Impact. International Journal of Impact Engineering 2007;34:89-103.

[8] Oshiro RE, Alves M. Scaling of Structures Subject to Impact Loads When Using a Power Law Constitutive Equation. International Journal of Solids and Structures 2009;46:3412-3421.

[9] Wei D, Hu C. Scaling of an Impacted Reticulated Dome Using Partial Similitude Method. Latin American Journal of Solids and Structures 2019;16(2):12.

[10] Oshiro RE, Calle MAG, Mazzariol LM, Alves M. Experimental Study of Collision in Scaled Naval Structures. International Journal of Impact Engineering 2017;110:149-161.

[11] Mazzariol LM, Oshiro RE, Alves M. A Method to Represent Impacted Structures Using Scaled Models Made of Different Materials. International Journal of Impact Engineering 2016;90:81-94.

[12] Alves M, Oshiro RE. Scaling Impacted Structures When the Prototype and the Model Are Made of Different Materials. International Journal of Solids and Structures 2006;43:2744-2760.

[13] Trimiño LF, Cronin DS. Non-Direct Similitude Technique Applied to the Dynamic Axial Impact of Bonded Crush Tubes. International Journal of Impact Engineering 2014;64:39-52.

[14] Mazzariol LM, Alves M. Similarity Laws of Structures under Impact Load: Geometric and Material Distortion. International Journal of Mechanical Sciences 2019;157-158:633-647.

[15] Mazzariol LM, Alves M. Experimental Verification of Similarity Laws for Impacted Structures Made of Different Materials. International Journal of Impact Engineering 2019;133:103364.

[16] Sadeghi H, Davey K, Darvizeh R, Darvizeh A. A Scaled Framework for Strain Rate Sensitive Structures Subjected to High Rate Impact Loading. International Journal of Impact Engineering 2019;125:229-245.

[17] Davey K, Darvizeh R, Al-Tamimi A. Scaled Metal Forming Experiments: A Transport Equation Approach. International Journal of Solids and Structures 2017;125:184-205.

[18] Sadeghi H, Davey K, Darvizeh R, Darvizeh A. Scaled Models for Failure under Impact Loading. International Journal of Impact Engineering 2019;129:36-56.

[19] Davey K, Darvizeh R. Neglected Transport Equations: Extended Rankine-Hugoniot Conditions and J-Integrals for Fracture. Continuum Mechanics and Thermodynamics 2016;28:1525-1552.

[20] Moghaddam M, Darvizeh R, Davey K, Darvizeh A. Scaling of the Powder Compaction Process. International Journal of Solids and Structures 2018;144-145:192-212.

[21] Al-Tamimi A, Darvizeh R, Davey K. Experimental Investigation into Finite Similitude for Metal Forming Processes. Journal of Materials Processing Technology 2018;262:622-637.

[22] Ochoa-Cabrero R, Alonso-Rasgado T, Davey K. Scaling in Biomechanical Experimentation: A Finite Similitude Approach. Journal of the Royal Society Interface 2018;15:0254.

[23] Lindholm US. High Strain-Rate Tests. Techniques in Metals Research, Vol. V, Part 1, R. Bunshad (ed.), Interscience, New York (1971).

[24] Tarigopula V, Langseth M, Hopperstad OS, Clausen AH. Axial Crushing of Thin-Walled High-Strength Steel Sections. International Journal of Impact Engineering 2006;32:847-882.

[25] Rajabiehfard R, Darvizeh A, Darvizeh M, Ansari R, Alitavoli M, Sadeghi H. Theoretical and Experimental Analysis of Elastic-Plastic Cylindrical Shells under Two Types of Axial Impacts. Thin-Walled Structures 2016;107:315-326.

[26] Karagiozova D, Jones N. On Dynamic Buckling Phenomena in Axially Loaded Elastic-Plastic Cylindrical Shells. International Journal of Non-Linear Mechanics 2002;37:1223-1238.

[27] Karagiozova D. Dynamic Buckling of Elastic-Plastic Square Tubes under Axial Impact-I: Stress Wave Propagation Phenomenon. International Journal of Impact Engineering 2004;30:143-166.

[28] Mirmohammadsadeghi SE, Khalili KH, Ahmadi SY, Hosseinipour SJ. Experimental and Finite Element Simulation Investigation of Axial Crushing of Grooved Thin-Walled Tubes. International Journal of Advanced Manufacturing Technology 2015;77:1627-1643.

[29] LSTC, LS-DYNA Keyword User's Manual. Volumes I to III (Version R7.1), Livermore Software Technology Corporation (LSTC). Livermore 2014.

[30] Karagiozova D, Alves M, Jones N. Inertia Effects in Axisymetrically Deformed Cylindrical Shells under Axial Impact. International Journal of Impact Engineering 2000;24:1083-1115.

[31] Karagiozova D, Jones N. Influence of Stress Waves on the Dynamic Progressive and Dynamic Plastic Buckling of Cylindrical Shells. International Journal of Solids and Structures 2001;38:6723-6749.

[32] Peixinho N, Doellinger C. Characterization of Dynamic Material Properties of Light Alloys for Crashworthiness Applications. Materials Research 2010;13:471-474.

[33] Yang X, Ma J, Sun Y, Yang J. An Internally Nested Circular-Elliptical Tube System for Energy Absorption. Thin-Walled Structures 2019;139:281-293.

[34] Vesenjak M, Hokamoto K, Anzel I, Sato A, Tsunoda R, Krstulovic-Opara L, Ren Z. Influence of the Explosive Treatment on the Mechanical Properties and Microstructure of Copper. Materials and Design 2015;75:85-94.